Petroleum Science 22 (2025) 1391–1406

Contents lists available at ScienceDirect

Petroleum Science

journal homepage: www.keaipublishing.com/en/journals/petroleum-science

Original Paper

Characteristics, controlling factors and mechanisms of natural fractures formation in lacustrine shale oil reservoirs: The Chang 7 member in Ordos Basin, China

Xiao-Yu Du [a], Zhi-Jun Jin [a, b, *], Lian-Bo Zeng [a, c], Guo-Ping Liu [a], Shi-Xiang Li [d], Mehdi Ostadhassan [e], Xin-Ping Liang [a], Guan-Ping Wang [b], Guo-Qing Lu [c]

[a] *Institute of Energy, Peking University, Beijing, 100871, China*
[b] *State Key Laboratory of Shale Oil and Gas Enrichment Mechanisms and Effective Development, SINOPEC, Beijing, 100083, China*
[c] *College of Geosciences, China University of Petroleum (Beijing), Beijing, 102249, China*
[d] *Research Institute of Exploration and Development, PetroChina Changqing Oilfield Company, Xi'an, 710018, Shaanxi, China*
[e] *Key Laboratory of Continental Shale Hydrocarbon Accumulation and Efficient Development, Ministry of Education, Northeast Petroleum University, Daqing, 163318, Heilongjiang, China*

A R T I C L E I N F O

Article history:
Received 18 July 2023
Received in revised form
12 October 2024
Accepted 3 March 2025
Available online 7 March 2025

Edited by Jie Hao and Meng-Jiao Zhou

Keywords:
Natural fractures
Mechanisms
Lacustrine shale
Chang 7
Ordos Basin

A B S T R A C T

Lacustrine shale oil reservoirs of the Upper Triassic Chang 7 Member in the Ordos Basin have demonstrated significant potential for hydrocarbon resources. Natural fractures play a crucial role in hydrocarbon enrichment and production. Outcrops, cores, borehole image logs, thin sections, and FE-SEM images were used to investigate the types and characteristics of natural fractures in the Chang 7 Member. The factors controlling fracture development and the mechanisms of bedding-parallel fracture formation were revealed by integrating TOC analysis, XRD analysis, and rock pyrolysis. Results show that natural fractures in the study area include high-angle tectonic fractures and nearly horizontal bedding-parallel fractures. Brittle minerals and bed thickness control the occurrence and attributes of tectonic fractures. High TOC content and thermal maturity positively affect the development of bedding-parallel fractures, formed through the conversion of organic matter to hydrocarbons or the smectite-to-illite transformation. Additionally, the dominant orientations of tectonic fractures intersect the present-day maximum horizontal principal stress at a small angle, resulting in large apertures and good effectiveness. Bedding-parallel fractures contribute to enhance porosity and provide favorable pathways for lateral hydrocarbon migration. Collectively, this study could provide valuable insights for finding promising exploration areas in lacustrine shale oil reservoirs in the Ordos Basin and worldwide.

1. Introduction

Lacustrine shales widely present in China have garnered significant attention in the field of unconventional energy (e.g., Zou et al., 2013; Yang et al., 2015, 2019; Li et al., 2019; Ju et al., 2020; Sun et al., 2021; Hou et al., 2022; Cao et al., 2023; Wang et al., 2023a, b; Zeng et al., 2023b), characterized by low porosity (<10%) and ultra-low permeability (<0.1 mD) (e.g., Jin et al., 2021; Liu et al., 2021d; Du et al., 2023a, b; Cao et al., 2024). The limited reservoir space and fluid conduits provided by matrix pores make the development of shale oil economically challenging, with natural fractures playing a significant role in hydrocarbon enrichment and production. Much work has documented natural fractures in tight sandstones, carbonate, and marine shales due to their influence on subsurface fluid flow and the response to hydraulic stimulation (Curtis, 2002; Cooke et al., 2006; Bowker, 2007; Gale et al., 2007, 2014; Ghosh and Mitra, 2009; Laubach et al., 2009; Ding et al., 2012; Jarvie, 2012; Gottardi and Mason, 2018; Lyu et al., 2019; Liu et al., 2020a, 2020b, 2021a, b, c, d).

Outcrops, cores, and borehole images are commonly used to identify fractures and measure their key attributes, such as fracture abundance, orientation, size (height, length, and aperture), and spatial distribution (Cooke et al., 2006; Laubach et al., 2009; Hooker

* Corresponding author.
E-mail address: jinzj1957@pku.edu.cn (Z.-J. Jin).

https://doi.org/10.1016/j.petsci.2025.03.005

et al., 2013; Gale et al., 2014; Gong et al., 2019; Lyu et al., 2019; Shi et al., 2020, 2023). A growing body of work has recently been published on the dominant controlling factors and formation mechanisms of natural fractures in marine shales. Numerous scholars have highlighted geological factors like sedimentation, diagenesis, and tectonics as the main controls on the development and distribution of fractures (Ding et al., 2012; Gale et al., 2014; Zeng et al., 2016; Zhang et al., 2020; Gong et al., 2021). The origin of fractures is generally attributed to regional and local stress changes associated with tectonic events (e.g., Gale et al., 2014), differential compaction during burial (e.g., Anders et al., 2014), hydrocarbon generation (e.g., Lash and Engelder, 2005), as well as uplift and exhumation (e.g., English, 2012). Despite these studies, systematic investigations have yet to be attempted regarding the characteristics, controlling factors, and mechanisms of natural fractures across lacustrine shale oil reservoirs, particularly concerning bedding-parallel fractures.

Significant progress has been made in shale oil exploration in the Chang 7 Member of the Ordos Basin (e.g., Yang et al., 2015; Cui et al., 2019; Ju et al., 2020). Exploration practices have demonstrated that the widespread natural fractures provide essential storage space and play a critical role in shale oil enrichment (Zhang et al., 2017; Fu et al., 2020). Although insights from the fractures in sandstones of the Yanchang Formation are relevant (e.g., Zeng et al., 2010; Zhao and Hou, 2017; Lyu et al., 2019), few studies have focused explicitly on fractures in lacustrine Chang 7 shales. Zhao and Hou (2017) established the relative timing of two fracture sets in the Yanchang Formation, showing that fractures developed in multiple orientations under different stress fields since the Late Triassic. Additionally, Zhang et al. (2017) identified three types of fractures in the Chang 7 Member and pointed out that microfractures are the predominant storage space for shale oil. However, there is still a lack of comprehensive studies on fracture characteristics and the factors governing fracture occurrence and attributes in the Chang 7 Member. Furthermore, different mechanisms of bedding-parallel fracture formation need more thorough investigation. Notably, several mechanisms of bedding-parallel fracture formation may act independently or in combination to cause fracture initiation, whereas they still need to be added to the best of our knowledge. A thorough understanding of fracture systems in the Chang 7 Member is crucial for effectively evaluating shale oil sweet spots within the Ordos Basin.

In this study, we identified and characterized two types of fractures using various datasets, including outcrops, cores, thin sections, borehole image logs, and field emission-scanning electron microscopy (FE-SEM). By integrating total organic carbon (TOC), X-ray diffraction (XRD) analysis, and rock pyrolysis data, we systematically demonstrated the main factors controlling fracture development. On this basis, we further discuss two mechanisms of bedding-parallel fracture formation and fracture effectiveness. The findings of this study could help delineate prolific regions and support the efficient development of lacustrine shale oil reservoirs within the Ordos Basin and globally.

2. Geological setting

The Ordos Basin, located in central China, is a typical multi-cycle superimposed petroliferous basin with abundant oil and gas resources (Zhang et al., 2017; Li et al., 2019; Jiu et al., 2022). It is surrounded by the Hetao Basin to the north, the North Qinlin Mountain to the south, the Helan Mountain and Liupan Mountain to the west, and the Lvliang Mountain to the east (Fig. 1(a)) (Lyu et al., 2019; Liu et al., 2021d). The overall shape of the basin is rectangular, covering an area of approximately 25×10^4 km^2 (Li et al., 2019; Jiu et al., 2022). Based on the current tectonic pattern, the Ordos Basin can be divided into six secondary tectonic units: the Western thrust belt, the Tianhuan Depression, the Yimeng Uplift, the Yishan Slope, the Jinxi fault-fold belt, and the Weibei Uplift (Fig. 1(a)) (Li et al., 2019; Xi et al., 2020; Liu et al., 2021b).

Due to the Indosinian movement in the late Triassic, the Yangtze Plate collided with the North China Plate, forming a large-scale inland depression in the Ordos Basin (Fu et al., 2020). The Ordos Block has undergone two tectonic events from the Late Mesozoic to the Cenozoic, leading to different tectonic regimes. From the Early Jurassic to the Late Cretaceous, the long-distance effects of subduction of the Izanagi Plate resulted in an NWW-trending stress field. Since the Paleogene, the collision between the Indian and Eurasian plates generated an NE-trending stress field (Zhao et al., 2016). Although the margin of the basin has undergone strong tectonic activities, the central part is relatively stable, characterized by small nose-shaped uplifts and an absence of faults and folds (Liu et al., 2021b; Ju et al., 2020).

The Upper Triassic Yanchang Formation consists of fluvial-lacustrine-delta terrigenous clastic sedimentary systems influenced by sediment sources from the southwest and northeast, which can be divided into Chang 1 Member to Chang 10 Member (Fu et al., 2020; Xi et al., 2020). The Chang 7 Member was deposited during the maximum flooding period and represents a semi-deep and deep lake area covering 6.5×10^4 km^2 (Fig. 1(a)) (Li et al., 2019; Fu et al., 2020; Liu et al., 2021d). Based on the sedimentary cycle and lithological features, the Chang 7 Member can be further divided into three sub-members from top to bottom, namely the Chang 7_1, Chang 7_2, and Chang 7_3 (Fig. 1(b)) (Liu et al., 2021a, 2021d). The Chang 7 Member holds significant shale oil resources and is the primary target for oil exploration in the Ordos Basin.

3. Databases and methods

3.1. Sample sources

In this study, 30 shale cores were collected from the Chang 7 Member of Well A, with continuous coring of 60 m (burial depth 190–250 m). The well is located in the Weibei Uplift of the Ordos Basin, northwest of Tongchuan City (Fig. 1(a)). All samples were analyzed for X-ray diffraction (XRD), total organic carbon (TOC) content and rock pyrolysis. Representative samples were selected for thin section and field emission-scanning electron microscopy (FE-SEM) observation. Additionally, the PetroChina Research Institute of Petroleum Exploration and Development provided detailed clay mineral composition data for Well A, spanning the Chang 4 + 5 Member to the Chang 9 Member. We also used published R_o and porosity data from previous studies (Wang et al., 2023a).

3.2. Field emission-scanning electron microscopy (FE-SEM)

FE-SEM observation was performed using an FEI Quanta 650 FEG with a maximum resolution of 10 nm, equipped with both secondary electron (SE) and backscattered electron (BSE) detectors. Initially, small pieces of rock samples (about 1 cm × 0.8 cm × 0.5 cm) were cut along the vertical bedding direction. The surface to be observed was then mechanically polished to the desired roughness and further polished for 1 h using a TechnoorgSC-100 argon-ion cross-section polisher. Subsequently, the polished surface was covered with gold and attached to the sample holder with conductive tape to enhance conductivity. Finally, an accelerating voltage of 25 kV, a 9–11 mm working distance, and a beam spot of 5.5 μm were used for further observations. The experiment was carried out at 20 °C and 40 % humidity.

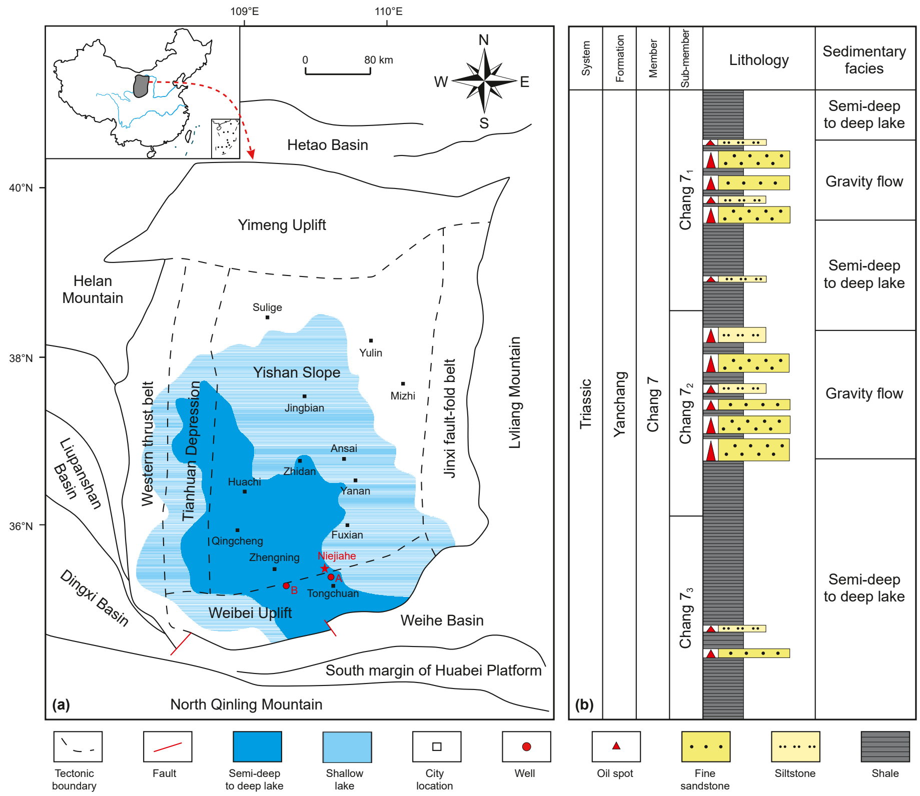

Fig. 1. **(a)** Tectonic units of the Ordos Basin, modified from Li et al. (2019) and Wang et al. (2023b). **(b)** Stratigraphic column of the Chang 7 Member in the Ordos Basin, modified from Fu et al. (2021).

3.3. X-ray diffraction (XRD) analysis

XRD analysis was performed using a Rigaku TTR X-ray diffractometer to quantitatively analyze the compositions of whole-rock and clay minerals. All testing procedures followed the Chinese Oil and Gas Industry Standard SY/T 5163-2010. The relative mineral percentage of the rock sample was determined by calculating the area under the curve of the main peak of each mineral and applying corrections for the Lorentz polarization (Chalmers et al., 2012).

3.4. Total organic carbon (TOC) analysis and Rock-Eval pyrolysis

TOC analysis was determined with a LECO CS230 carbon and sulfur analyzer. The experiments were conducted according to the Chinese National Standard GB/T 19145-2003. Pyrolysis analysis was performed using the Rock-Eval 6 instrument. Initially, the sample was heated at a constant temperature of 300 °C for 3 min to obtain S_1 (free hydrocarbons). Then, the temperature was increased at 25 °C/min up to 650 °C to obtain S_2 (pyrolysis hydrocarbons) and T_{max} (temperature of maximum pyrolysis yield), in accordance with the Chinese Standard GB/T 18602-2012.

3.5. Fracture characterization

Facture characterization was conducted using various datasets of outcrops, cores, borehole image logs, and thin sections. The outcrop is located in Niejiahe Village, Yaoqu Town, Tongchuan City, Shaanxi Province (Fig. 1(a)). Since weathered fractures in the outcrop must be excluded, only straight, evenly spaced, and extensively propagated fractures were selected for investigation. Core observation was conducted at the core library of PetroChina Changqing Oilfield Company. Borehole image interpretation of Well B was performed using Schlumberger's Techlog software. Thin section observation was conducted at the Institute of Energy, Peking University, using a LEICA DM4P polarizing microscope.

We identified and characterized the multi-scale fractures in the Chang 7 Member based on different datasets. Outcrops, cores, and borehole images were used to study the macroscopic characteristics of the fractures, while thin sections and scanning electron micrographs were prepared for microanalysis. Generally, fractures observed in outcrops range from centimeters to meters in height. In contrast, fractures in cores and borehole images are typically at the centimeter scale, while those in thin sections and FE-SEM images are at the micron scale.

Fracture attributes, including orientation, dip angle, height, filling, and density, were determined using the abovementioned data. Fracture orientation and dip angle were derived from borehole image log interpretation. Fracture height in cores was measured using a meter ruler. Considering borehole image logs, the well was drilled with conductive mud. Thus, fractures appear bright when they contain minerals and dark when open and not filled (e.g., Aghli et al., 2019; Lyu et al., 2019). Fracture density is defined as the number of fractures per unit length (e.g., Ortega et al., 2006), using the vertical wellbore as scanlines.

4. Results

4.1. Lithology and mineralogy

Through detailed core observation and thin section analysis, five lithologies are identified in the Chang 7 Member: fine sandstone, siltstone, muddy siltstone, silty mudstone, and mudstone. The Chang 7_1 and Chang 7_2 sub-members are dominated by sandstones, which are vertically interbedded with source rocks and exhibit good oil content. In contrast, the Chang 7_3 sub-member is predominantly composed of mudstone.

XRD data indicates that the Chang 7 Member is rich in clay minerals and quartz, with an average content of 34.00 w.t.% and 27.80 w.t.%, respectively (Fig. 2(a)). Clay minerals are dominated by mixed-layer illite/smectite (I/S), with an average content of 80.17 w.t.%, followed by small amounts of illite, chlorite and kaolinite (Fig. 2(b)), indicating that the diagenesis sequence is in the middle diagenetic stages. Furthermore, pyrite comprises a relatively high proportion, with an average content of 17.90 w.t.%. The contents of feldspar and carbonate minerals are relatively low, with average contents lower than 10 w.t.% (Fig. 2(a) and (c)).

4.2. TOC content and Rock-Eval pyrolysis

TOC values of all samples range from 0.62 w.t.% to 26.90 w.t.%, with an average of 9.34 w.t.% (Fig. 2(d)). Rock-Eval T_{max} values range from 434 to 447 °C (avg. 439 °C), with 93% of values below 450 °C. The hydrogen index (HI) varies from 66 mg HC/g TOC to 540 mg HC/g TOC (avg. 345 mg HC/g TOC), showing a general decreasing trend with increasing T_{max} (Fig. 3). Therefore, the studied samples are in low-maturity to maturity stage. The T_{max} versus hydrogen index (HI) cross-plot was utilized to evaluate the organic matter types. The result shows that the samples primarily comprise type II kerogen, with type II_1 and type II_2 accounting for 53% and 30%, respectively. Type I kerogen represents only 17% (Fig. 3). Thus, the Chang 7 shales are characterized by mixed kerogen types with oil-prone generation potential.

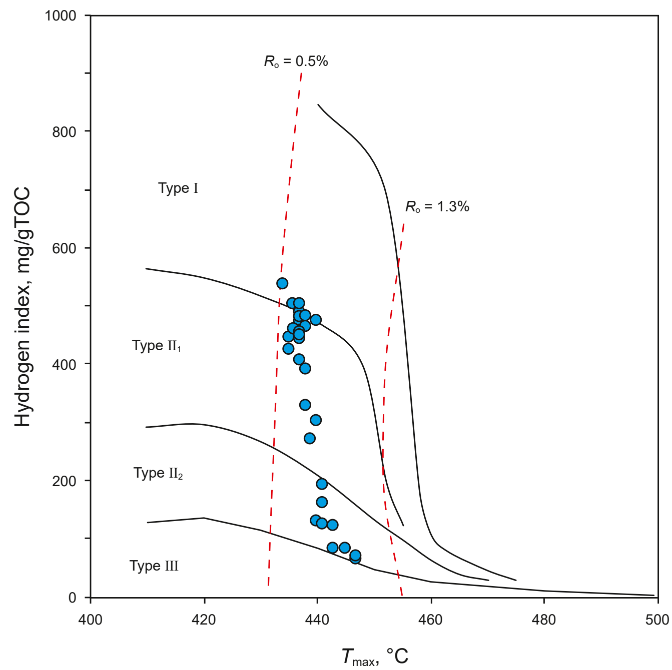

Fig. 3. Cross-plot of T_{max} versus hydrogen index (HI) showing organic matter type and thermal maturity.

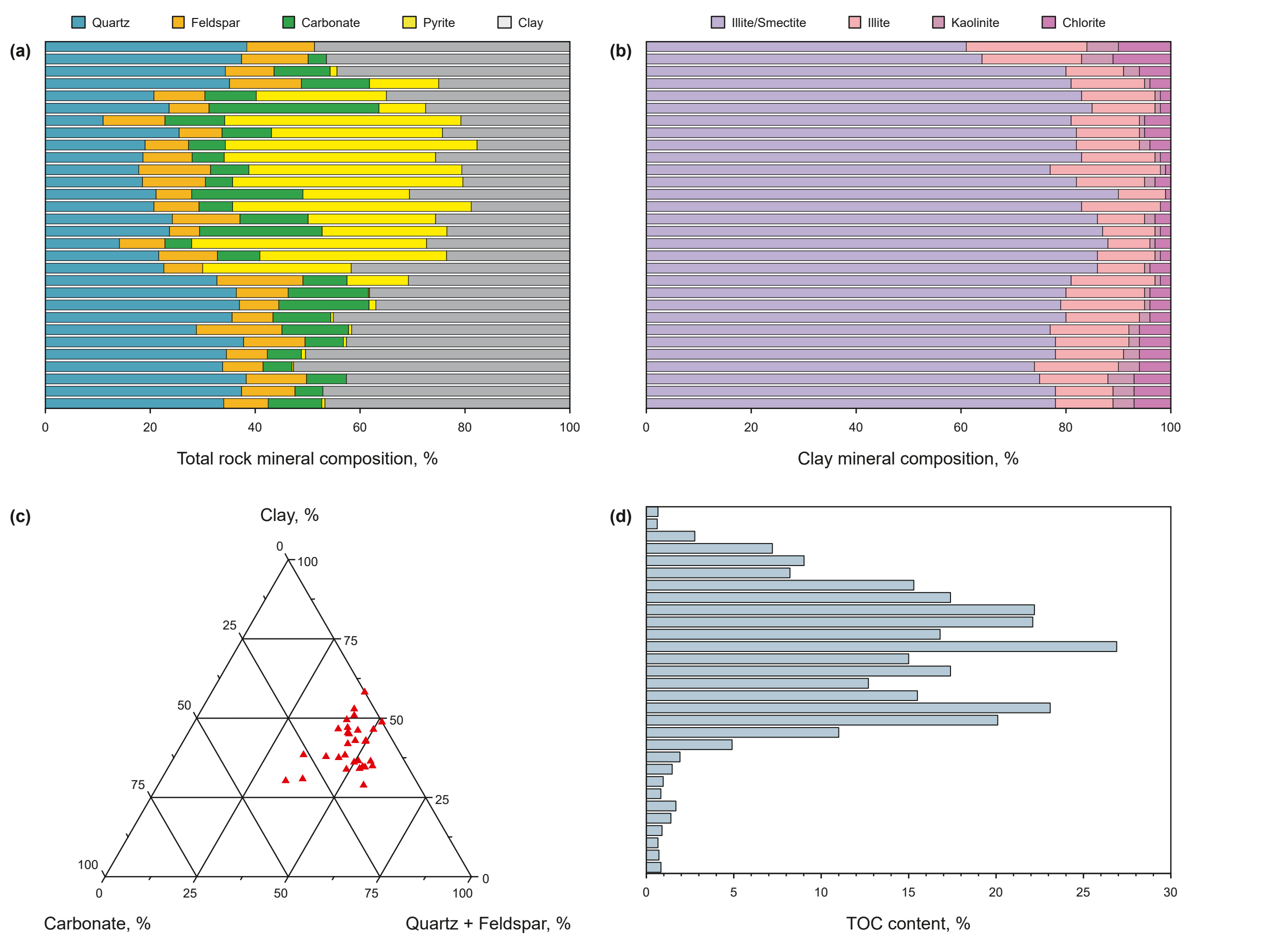

Fig. 2. Mineralogy and TOC results of the Chang 7 Member in Well A. **(a)** Whole-rock composition. **(b)** Clay mineral composition. **(c)** Mineralogical ternary diagram. **(d)** TOC content.

4.3. Fracture types and characteristics

Observations confirm that natural fractures are widespread in the Chang 7 Member of the Ordos Basin. Based on geological characteristics and distribution features, natural fractures can be classified into high-angle tectonic fractures and nearly horizontal bedding-parallel fractures (Figs. 4–8). Our study focuses on these two fracture types.

4.3.1. Tectonic fractures

Numerous tectonic fractures perpendicular to bedding are present in outcrops, cores, and borehole images (Figs. 4–6), formed under paleotectonic stress fields during various geologic times. Fractures in outcrops usually terminate at bedding planes and are evenly spaced, with varying degrees of development across different strata (Fig. 4(a)). The majority of fractures in cores are nearly vertical or inclined at angles of 60°–80° relative to bedding (Fig. 5(a)–(e)), and multiple groups of fractures intersect each other (Fig. 5(d) and (e)). Some fractures are filled with minerals such as calcite and quartz (Fig. 5(c)). Additionally, crude oil can be observed on some fracture surfaces, denoting that these fractures played a significant role in hydrocarbon migration and accumulation (Fig. 5(a)).

Borehole image log interpretations show that NE-SW striking fractures are the most abundant, with a few fractures oriented in other directions also present (Fig. 6(a)). The dip angles of tectonic fractures mainly range from 70° to 90°, accounting for a total percentage of 96% (Fig. 6(b)). Tectonic fractures are generally minor in size, with core fracture heights typically less than 10 cm (Fig. 6(c)). The degree of fracture development in the Chang 7 Member is relatively high, with a fracture density of 2.65 m^{-1} in Well B. Furthermore, tectonic fractures in the Chang 7_1 Member and Chang 7_2 Member are more developed vertically than those in the Chang 7_3 Member (Fig. 6), with fracture densities of 4.92, 3.23, and 0.80 m^{-1}, respectively.

4.3.2. Bedding-parallel fractures

Bedding-parallel fractures are abundant in the Chang 7 shale oil reservoirs. This study defines bedding-parallel fractures as natural fractures that occur along or nearly parallel to the sedimentary bedding planes. Bedding-parallel fractures in cores are typically roughly parallel to the bedding planes. Each fracture has a short lateral extension and a discontinuous distribution, usually less than the width of the core (Fig. 5(f)–(i)). Due to the small apertures, it is often necessary to wet the core surface to observe them clearly (Fig. 5(g) and (i)). In sandstone, bedding-parallel fractures are relatively less developed and exhibit a straight, horizontal distribution. Different fractures are arranged in parallel with varying lateral extensions, typically within a few centimeters. In muddy siltstone, the orientation of bedding-parallel fractures varies significantly, often displaying a curved pattern along the laminae. These fractures are more commonly found near organic matter laminae and are more extensively developed. Mudstone has the highest development of bedding-parallel fractures, with some filled with minerals. Fig. 5(h) shows bedding-parallel fractures filled with fibrous calcite, where the calcite veins are thick but poorly continuous, locally appearing in en-echelon arrays.

Bedding-parallel fractures are mostly curved in thin sections and mainly develop around hard mineral grains and along grain edges (Fig. 7(a)–(e)). They usually occur at the boundaries or within organic-rich laminae (Fig. 7(a)–(e)), with apertures of less than 10 μm (Fig. 7(a)–(d)). Some bedding-parallel fractures are also mineral-filled, presenting lenticular shapes that taper from the center towards the edges (Fig. 7(f)). FE-SEM images show bedding-parallel fractures near organic matter or within clay minerals, displaying features such as branching, bending, or pinching out (Fig. 8). Additionally, they tend to be more prevalent at boundaries between organic matter and inorganic minerals (especially pyrite framboids) (Fig. 8(b)–(e), (h) and (i)). Notably, numerous bedding-parallel fractures are present in the organoclay complexes of Chang 7 shales (Fig. 8(d)). Single bedding-parallel fractures usually have limited extension and pinch out away from organic matter (Fig. 8(b)–(d), and (i)). The development of bedding-parallel fractures in shale oil reservoirs exhibits strong heterogeneity, with apertures varying significantly, sometimes differing by several orders of magnitude across fractures or even along the same fracture. The maximum aperture can reach several tens of micrometers (Fig. 7(e)), while the minimum aperture is only a few hundred nanometers (Fig. 8(b)–(d), (f), (h) and (i)). Nevertheless, bedding-parallel fracture apertures are larger than the macropore size standard, making them effective storage spaces and flow channels for hydrocarbons. Bedding-parallel fracture surfaces observed in cores are rough and uneven, with visible residual oil indicating they were open and effective underground (Fig. 5(j)).

5. Discussion

5.1. Factors controlling fracture development

5.1.1. Lithology and mineral composition

Studies have demonstrated that rock composition affects the development of natural fractures (e.g., Ding et al., 2012; Gale et al., 2014; Ghosh et al., 2018; Jiang et al., 2023). The relationship between brittle mineral content and tectonic fracture density was diagrammed. It is evident that fractures occur in the Chang 7 Member when the brittle mineral content exceeds 70 w.t.%, with

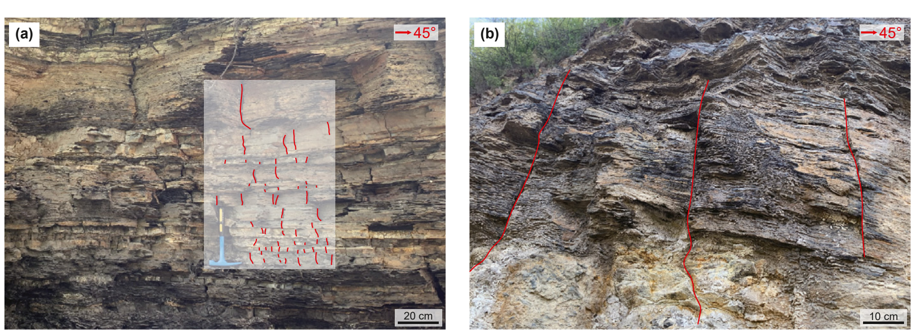

Fig. 4. Tectonic fractures of the Chang 7 Member in the outcrop near Niejiahe Village, Yaoqu Town. **(a)** Intralayer fractures. **(b)** Trans-layer fractures.

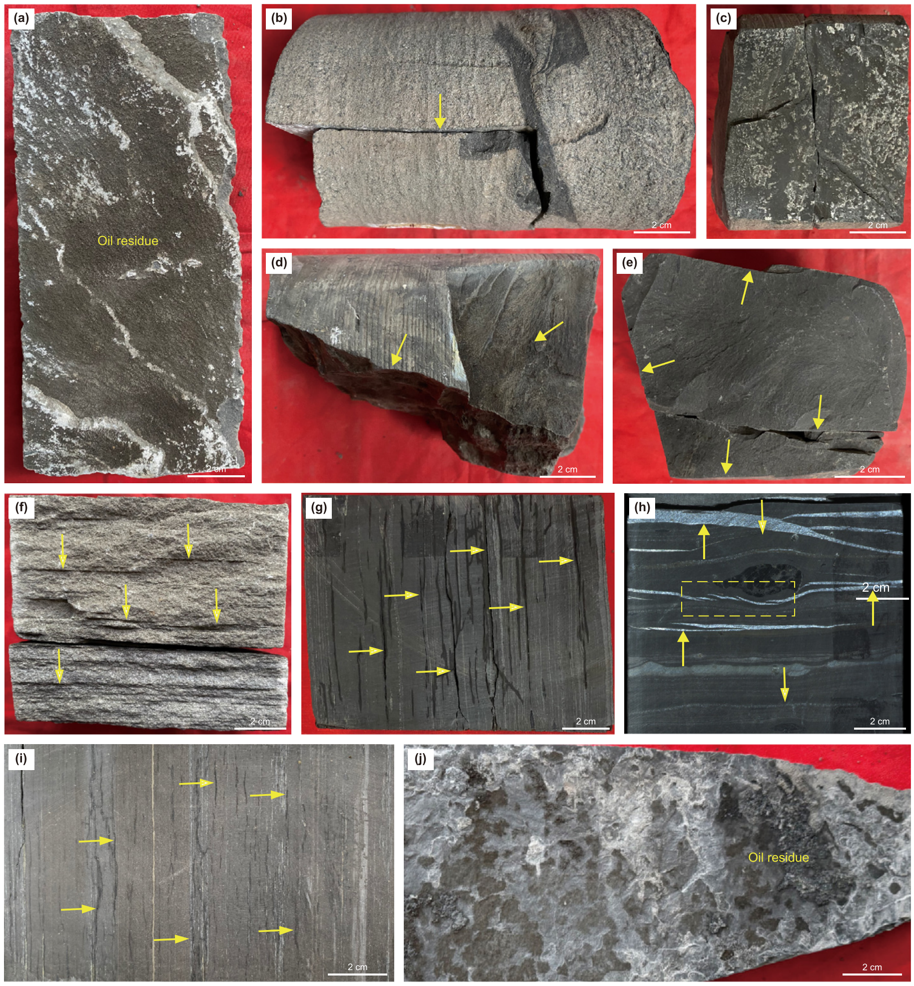

Fig. 5. Natural fractures in cores in the Chang 7 Member of the Ordos Basin. **(a)** Crude oil can be observed on the surface of nearly vertical tectonic fractures. **(b)** Nearly vertical tectonic fractures terminate in mudstone. **(c)** Tectonic fracture is partially filled with calcite. **(d)** Two sets of tectonic fractures. **(e)** Two sets of tectonic fractures. **(f)** Bedding-parallel fractures in sandstone. **(g)** Bedding-parallel fractures in mudstone. **(h)** Bedding-parallel fractures are filled with fibrous calcite veins arranged in en-echelon patterns in some areas. **(i)** Bedding-parallel fractures in silty mudstone. **(j)** Crude oil can be observed on the surface of bedding-parallel fractures.

fracture density positively correlated with the mass percentage of brittle minerals (Fig. 9(a)). Shales with high brittle content (such as quartz, feldspar, and carbonate) have higher Young's modulus and lower Poisson's ratio, making them more likely to fracture under external forces (Gale et al., 2014; Du et al., 2023a). Conversely, shales containing a high proportion of clay minerals or organic matter tend to display more ductile behavior and relatively high strain at failure, which make them less prone to fracture (Altindag, 2010).

Outcrop and core observations show that tectonic fractures tend to be concentrated in fine sandstone and siltstone. This can be attributed to the high brittle mineral content in sandstone. Siltstone exhibits the highest degree of fracture development among all lithologies, with a fracture density of 1.88 m^{-1} (Fig. 10(a)). This is because siltstone is not only rich in brittle mineral but is also strongly cemented by calcite (Fig. 10(b)). Additionally, a general tendency is evident that brittle mineral grains in contact are likely to have a more significant effect on increasing brittleness than isolated grains (Gale et al., 2014). Compared to siltstone, fine sandstone displays a lower abundance of fractures correspondingly (Fig. 10(a)), likely due to its larger grain size and higher porosity. An increase in rock porosity leads to a rise in strain at failure and, ultimately decreasing brittleness (Heidari et al., 2013). In addition, due to the high content of brittle minerals, the tectonic fractures are more developed in the Chang 7_1 Member and Chang 7_2 Member, which are dominated by sandstone (Fig. 9(b)).

5.1.2. Mechanical stratigraphy

Shales are typically layered sedimentary rocks with marked mechanical anisotropy due to thin beds, laminae, and bedding-parallel fabric (i.e., oriented alignment of plate-like clay minerals) (Day-Stirrat et al., 2008; Gale et al., 2014; Du et al., 2023a). Mechanical stratigraphy refers to the subdivision of rock into discrete intervals with similar mechanical properties (i.e., brittleness, elastic stiffness, tensile strength, and fracture mechanics) governed by depositional, diagenetic, and structural settings (Cooke et al., 2006; Laubach et al., 2009; McGinnis et al., 2017). Mechanical stratigraphy controls the deformation behavior of the rock and determines its response to applied forces, which in turn affects natural fracture development. Thus, fracture attributes depend on mechanical stratigraphy. Outcrops show that tectonic fractures typically occur within individual rock layers and terminate at rock interfaces (Fig. 4(a)). Cores also show that fractures extend in siltstone (brittle layer) and terminate at mudstone (ductile layer) (Fig. 5(b)).

Different rock interfaces and types constitute mechanically distinct boundaries and intervals. We use the height hierarchy

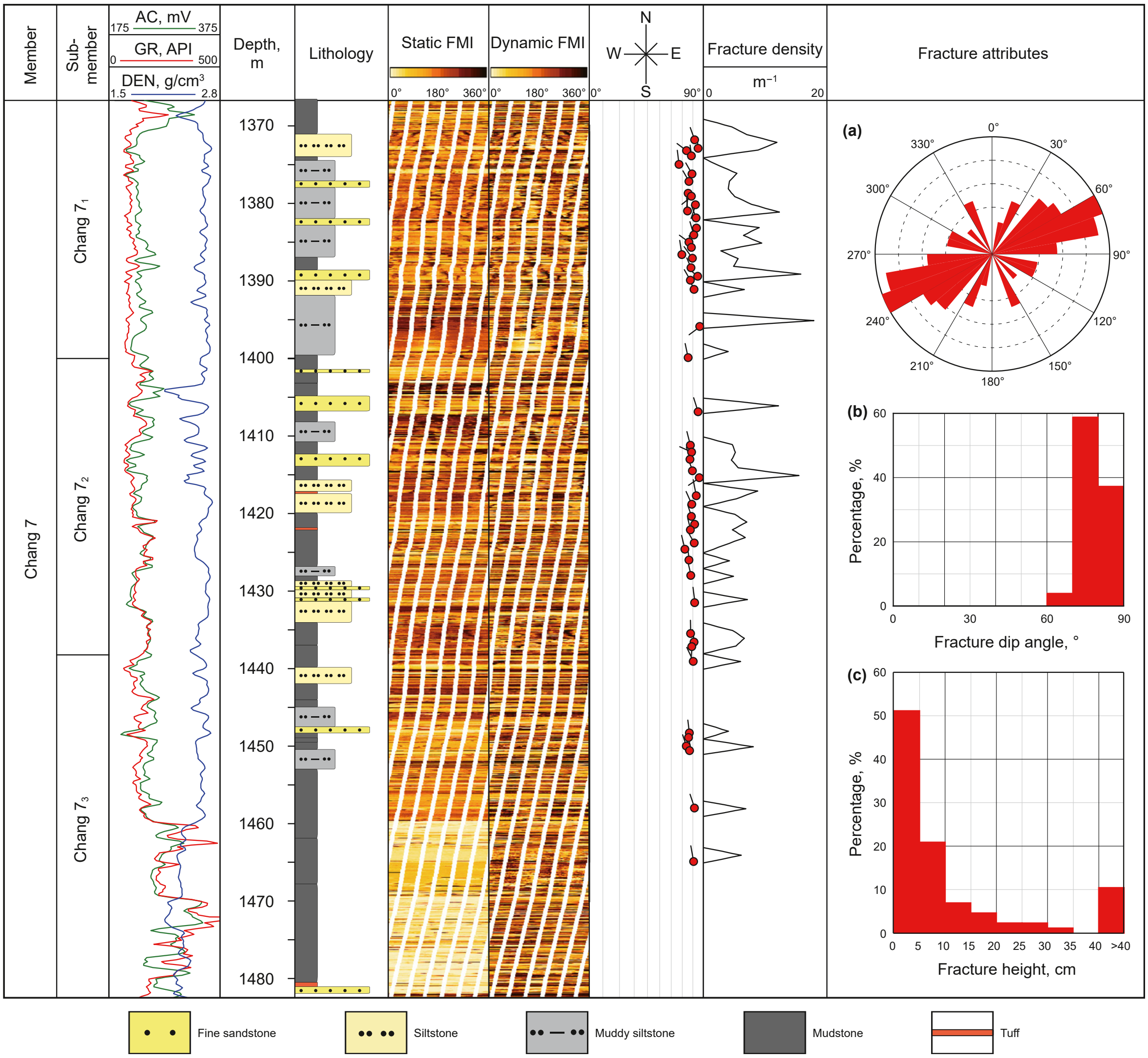

Fig. 6. Tectonic fractures identified by borehole image logs and fracture parameters in Well B of the Ordos Basin. **(a)** Fracture orientation. **(b)** Fracture dip angle distribution. **(c)** Fracture height distribution.

classification proposed by Hooker et al. (2013, their Fig. 5), which categorizes fractures based on their configuration relative to bed boundaries. Results show that fracture heights in the Chang 7 Member generally follow hierarchical patterns. This arrangement arises because fractures are bounded by a variety of interbedded layers, resulting in a series of vertical fractures. The fracture tips with specific heights terminate at specific interfaces, while arrays of fractures with varying heights overlap in nested layers. Furthermore, we found that fracture abundance is controlled by bed thickness. A negative correlation exists between fracture density and bed thickness, following a power function in the Chang 7 Member (Fig. 11). A possible explanation for this pattern is that the thinner rock layers are more prone to fracture under equivalent applied forces. The excellent relationship between fracture spacing and bed thickness, as described by Laubach et al. (2009), further supports this observation.

Additionally, some small-scale faults or trans-layer fractures observed in outcrops cut through multiple rock layers (Fig. 4(b)), which were unaffected by mechanical layers. These trans-layer fractures are fault-related fractures, formed in conjunction with the faults. The significant local tectonic stress around the faults resulted in larger-scale fractures with greater extension, thus allowing them to span multiple strata.

5.1.3. *TOC content and thermal maturity*

TOC content is a critical factor influencing the development of bedding-parallel fractures under the same tectonic setting and sedimentary environment (Ding et al., 2012; Ougier-Simonin et al., 2016; Wang et al., 2016). The TOC content of the Chang 7 shales is relatively high compared to other continental shales in China, reaching up to 26.9 w.t.%. Higher TOC content corresponds to a greater density of bedding-parallel fractures (Fig. 12(a)), indicating that high TOC promotes the development of bedding-parallel fractures. This phenomenon is related to the local overpressure caused by organic-rich shales during hydrocarbon generation, which will be discussed in detail in Section 5.2. Additionally, we found that when the TOC content is below 5 w.t.%, the density of bedding-parallel fractures increases rapidly with rising TOC content. However, once the TOC content exceeds 5 w.t.%, the increase rate in fracture density gradually slows down. When the TOC content surpasses 20%, the fracture density stabilizes at about 100 m^{-1}.

Thermal maturity is another key factor affecting the

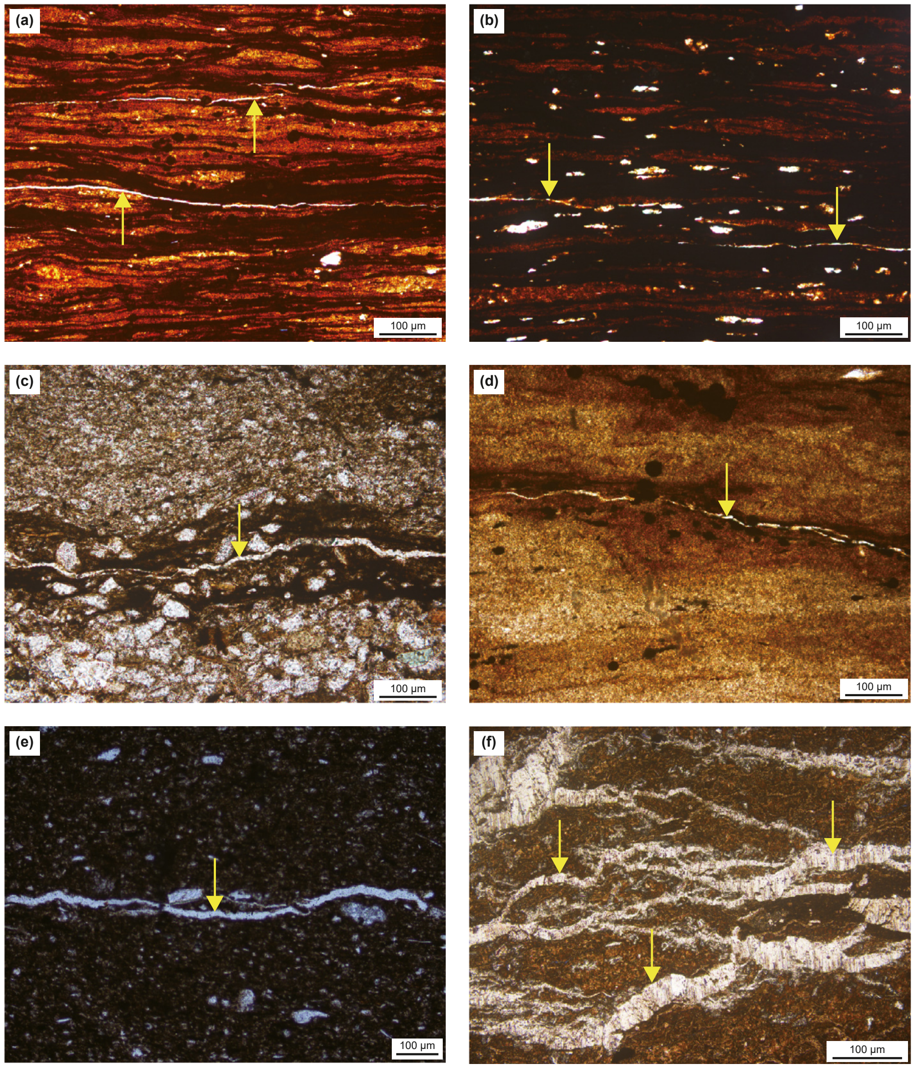

Fig. 7. Bedding-parallel fractures in thin sections in the Chang 7 Member of the Ordos Basin. **(a)** Bedding-parallel fractures along the edges of organic-rich laminae. **(b)** Bedding-parallel fractures within organic-rich laminae. **(c)** Bedding-parallel fractures within organic-rich laminae. **(d)** Bedding-parallel fractures within clay laminae. **(e)** Bedding-parallel fractures bypassing hard mineral particles. **(f)** Filled bedding-parallel fractures.

development of bedding-parallel fractures. To avoid the impact of TOC content, we introduced the normalized bedding-parallel fracture density (100 × original bedding-parallel fracture density/TOC content). When the T_{max} values are below 438 °C, the normalized bedding-parallel fracture density is less than 10 m^{-1}. However, when the T_{max} values exceed 438 °C, the fracture density begins to increase significantly and shows a positive correlation with T_{max}, indicating that the thermal evolution of organic matter promotes fracture formation (Fig. 12(b)). Additionally, the fitting curve between TOC content and bedding-parallel fracture density reveals a clear trend: initially steep, then gradually leveling off (Fig. 12(a)). This occurs because samples with TOC values below 5 w.t.% have higher maturity (average T_{max} of 442 °C), whereas samples with TOC values above 5 w.t.% have lower maturity (average T_{max} of 437 °C).

Furthermore, statistical analysis shows a strong positive correlation between organic carbon abundance and pyrite content. This relationship arises because pyrite indicates a highly reducing, anoxic environment during the deposition of the Chang 7 Member, characterized by high primary productivity, low sedimentation rates, volcanic activity, and hydrothermal processes (Chen et al., 2020; Liu et al., 2021a). These factors significantly contributed to organic matter enrichment. Consequently, the density of bedding-parallel fractures is positively correlated with pyrite content.

5.1.4. Laminae type

Studies have pointed out a strong association between bedding-parallel fractures and laminae (e.g., Lai et al., 2022; Pang et al., 2023; Zeng et al., 2023a). The Chang 7 Member exhibits various types of laminae, including organic-rich, clay, tuff-rich, and feldspar-quartz laminae. Bedding-parallel fractures observed in cores, thin sections, and FE-SEM images are typically oriented approximately parallel to the laminae interfaces and are more developed in densely laminated layers (Fig. 13(a) and (b)). A possible explanation might be that different laminae have the distinct physical and chemical properties that create mechanical discontinuities at the contact interface (Lash and Engelder, 2005). Such a change in interlayer atomic bonds creates contrasting stress fields (Ougier-Simonin et al., 2016), making the laminae interfaces favorable sites for initiating bedding-parallel fractures. Furthermore, the presence of bedding-parallel fractures in different laminae was examined. Result reveals that bedding-parallel

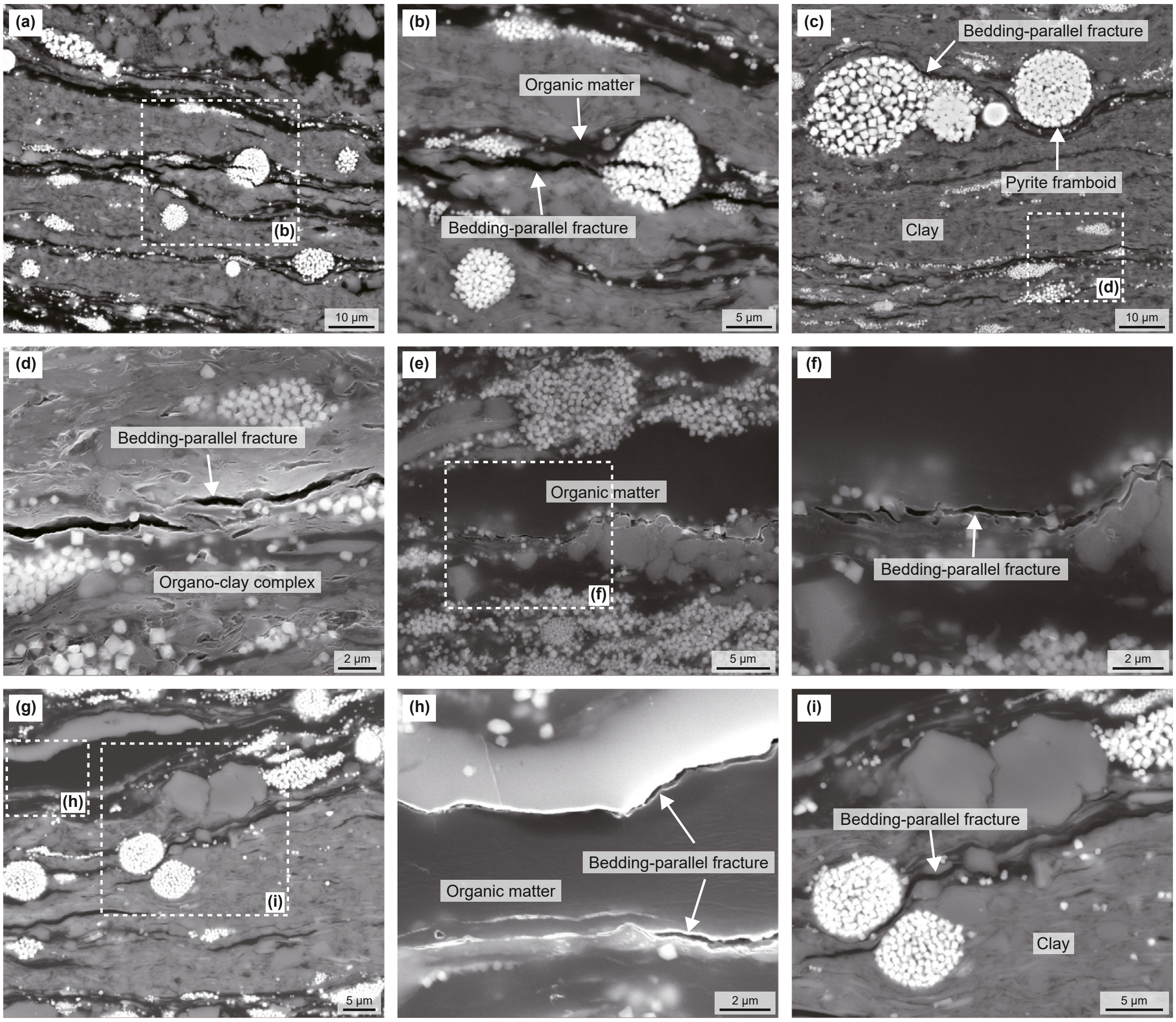

Fig. 8. Bedding-parallel fractures in FE-SEM images in the Chang 7 Member of the Ordos Basin. **(a)** Multiple bedding-parallel fractures aligned approximately in parallel, BSE image. **(b)** En-echelon bedding-parallel fractures near the organic matter, BSE image. **(c)** Bedding-parallel fractures bypassing pyrite framboids, BSE image. **(d)** Bedding-parallel fractures developed within organo-clay complexes, SE image. **(e)** Bedding-parallel fractures at the boundary between organic matter and inorganic minerals, BSE image. **(f)** Bedding-parallel fractures within organic matter, BSE image. **(g)** Multiple bedding-parallel fractures associated with organic matter and clay, BSE image. **(h)** Bedding-parallel fractures at the edge of organic matter, SE image. **(i)** Bedding-parallel fractures between different laminae, BSE image.

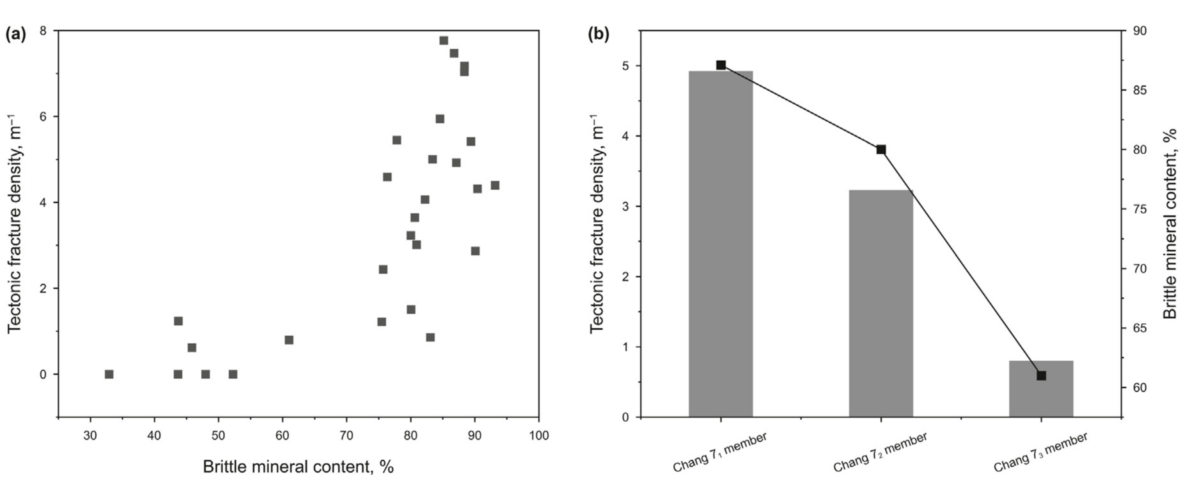

Fig. 9. **(a)** Relationship between tectonic fracture density and brittle mineral content. **(b)** Distribution of tectonic fracture density and brittle mineral content in Chang 7 sub-member.

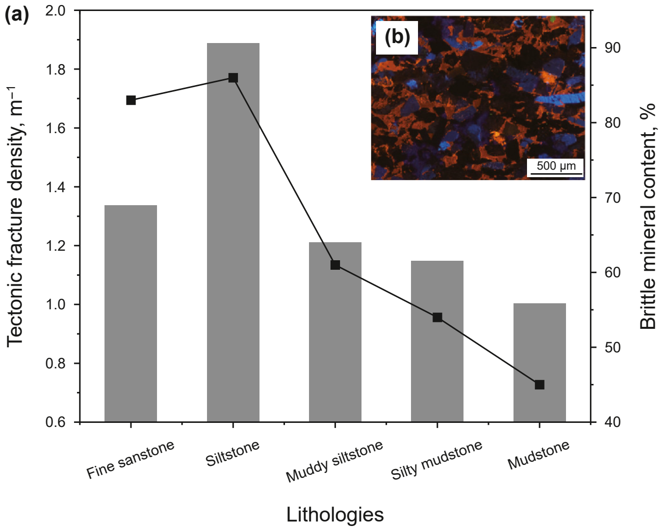

Fig. 10. **(a)** Distribution of tectonic fracture density and brittle mineral content among different lithologies. **(b)** Cathodoluminescence image of strongly cemented siltstone (orange color indicates calcite cementation).

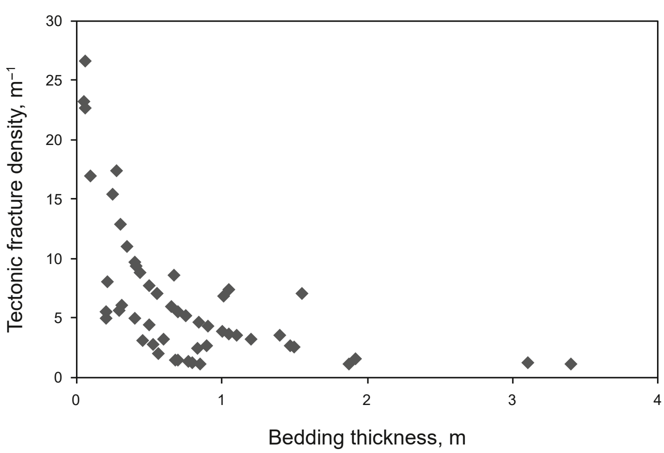

Fig. 11. Relationship between tectonic fracture density and bed thickness.

fractures are most likely to appear in organic-rich laminae (accounting for 51%), followed by clay laminae (accounting for 28%). However, fewer bedding-parallel fractures occur in tuff-rich and feldspar-quartz lamina, with percentages of 13% and 8%, respectively. This is attributed to the high TOC content in the organic-rich laminae, which are frequently interbedded with clay laminae (Fig. 13(c) and (d)).

5.2. Mechanisms of bedding-parallel fractures

5.2.1. The conversion of organic matter to hydrocarbons

Many nearly horizontal bedding-parallel fractures are observed in cores, thin sections, and FE-SEM images (Figs. 5(f)–(i), 7(a)–(e) and 14(a)–(b)). High-magnification images reveal that these bedding-parallel fractures are composed of multiple microfractures developed near the organic matter at the microscopic level (Figs. 8(b)–(d), (f) and 14(c)). This suggests that the formation of bedding-parallel fractures is closely associated with the presence of organic matter. Our findings align with recent studies. The Chang 7 shales exhibit a very high TOC content, with kerogen predominantly of types II_1 and II_2, along with a small amount of type I (Fig. 3), indicating excellent potential for hydrocarbon generation (Yang et al., 2015; Fu et al., 2020). Furthermore, the thermal maturity of the source rocks is moderate, with vitrinite reflectance (R_o) exceeding 0.5% (Fig. 3), suggesting the shales have just entered the oil window. The thermal evolution of organic matter in Chang 7 shales promotes the formation of bedding-parallel fractures. Therefore, we found that bedding-parallel fractures are positively correlated with thermal maturity (T_{max}) (Fig. 12(b)).

As the organic matter matures, the conversion of high-density solid kerogen to lower-density liquid oil leads to local volume expansion due to the significant increase in fluid production exceeding the volume reduction of kerogen, generating abnormally high pressure (Fig. 14(e)) (Momper, 1979; Fan et al., 2010; Ougier-Simonin et al., 2016; Yang and Mavko, 2018; Meng et al., 2021). Previous studies have documented overpressure in the Chang7 Member, with residual pressures ranging from 8 to 16 MPa (Yao et al., 2018; Fu et al., 2020; Liu et al., 2021c). These local overpressures partially relieve the overlying load, reducing the effective stress within the solid framework. When the pore-fluid pressure balances the lithostatic stress of the overlying strata, all effective

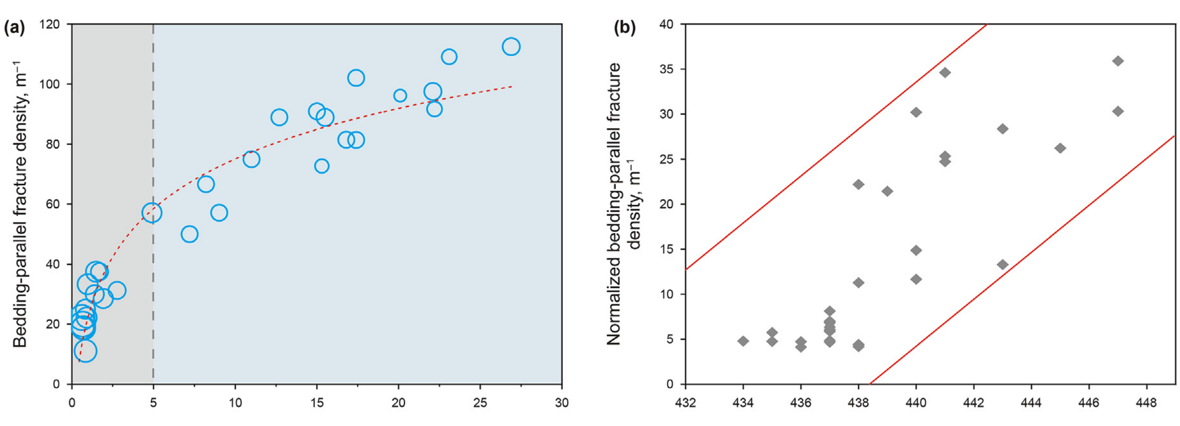

Fig. 12. **(a)** Relationship between TOC content and bedding-parallel fracture density (The size of the bubbles indicates the T_{max} value, with the gray area representing higher T_{max} values and the light blue area indicating lower T_{max} values). **(b)** Relationship between T_{max} and bedding-parallel fracture density.

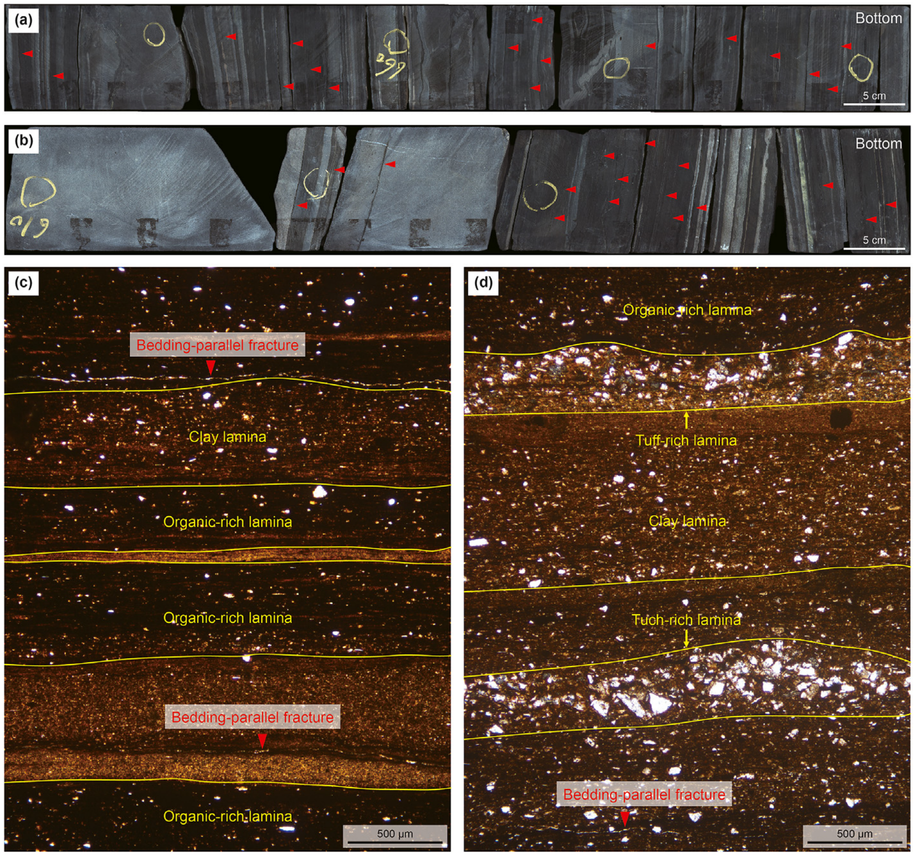

Fig. 13. Laminae types and bedding-parallel fractures of the Chang 7 Member in the Ordos Basin. ((**a**)–(**b**)) Bedding-parallel fractures in cores, red triangles indicating bedding-parallel fractures. ((**c**)–(**d**)) Bedding-parallel fractures in thin sections.

stresses are eliminated. With even greater overpressure, the vertical effective stress transforms into tensile stress.

The flattened shape of kerogen particles and the strength anisotropy of laminated shale promote the decoupling between lenticular kerogen and surrounding mineral particles (Lash and Engelder, 2005; Ougier-Simonin et al., 2016), facilitating the initiation of horizontal microfractures along weak bedding surface. Additionally, due to the extremely low fracture toughness of the organic matter (Vernik, 1994), microfractures tend to initiate at the boundaries between kerogen or kerogen-clay minerals when pore pressure slightly exceeds vertical stress. Once the Mohr circle intersects the failure envelope, rock failure occurs, leading to the formation of horizontal microfractures (Cobbold et al., 2013). These multiple microfractures interconnect horizontally, eventually forming bedding-parallel fractures within the shale (Fig. 14(d) and (f)).

5.2.2. The transformation of smectite to illite

Numerous studies have suggested that bedding-parallel fractures may be linked to the transformation of clay minerals during diagenesis (Powers, 1967; Bruce, 1984; Zhao and He, 2012; Ougier-Simonin et al., 2016; Wang et al., 2016; Yang and Mavko, 2018; Meng et al., 2021). The vertical distribution of clay minerals in Well A shows that the proportion of mixed-layer illite/smectite in the Chang 7 Member is significantly increased, while the contents of illite, kaolinite and chlorite are relatively low (Fig. 15). Based on the composition and proportion of clay minerals, as well as the thermal maturity, the diagenetic evolution of the Chang 7 Member has reached the middle diagenetic stage A (Zhao and He, 2012). Statistical analysis shows a positive correlation between bedding-parallel fractures and the proportion of mixed-layer illite/smectite (Fig. 16), indicating that clay mineral transformations promote the formation of bedding-parallel fractures. Two mechanisms may explain this phenomenon. First, the transformation of smectite to illite during diagenesis converts bound water into free water. Since bound water has a higher density than free water, this transformation leads to an increase in fluid volume, contributing to overpressure in shale reservoirs (Powers, 1967; Bruce, 1984; Zhao and He, 2012; Qin et al., 2019; Meng et al., 2021).

Furthermore, the burial process significantly alters the composition and structure of clay minerals in shales (Bruce, 1984; Capuano, 1993; Zhao and He, 2012; Meng et al., 2021). As underground temperature and pressure increase, smectite undergoes chemical reactions such as dehydration and ion exchange (Al-Ramadan, 2013; Qin et al., 2019), gradually transforming into plate-like illite. The weak electrostatic interactions between hydrated ions and other metal ions in the interlayer of smectite result in larger basal layer spacing. In contrast, the stronger hydrogen bonding and van der Waals forces in illite result in reduced interlayer spacing within the plate-like structure. Consequently, this change in crystal structure causes a reduction in volume. The smectite-to-illite transformation in shales leads to volumetric contraction, which generates localized tensile stresses and eventually small-scale tensile fractures. When multiple independent tensile fractures expand, propagate, and interconnect, they form bedding-parallel fractures. These bedding-parallel fractures of this origin typically exhibit short extensions and variable apertures and are often distributed around mineral particles such as pyrite (Fig. 8(d) and (i)).

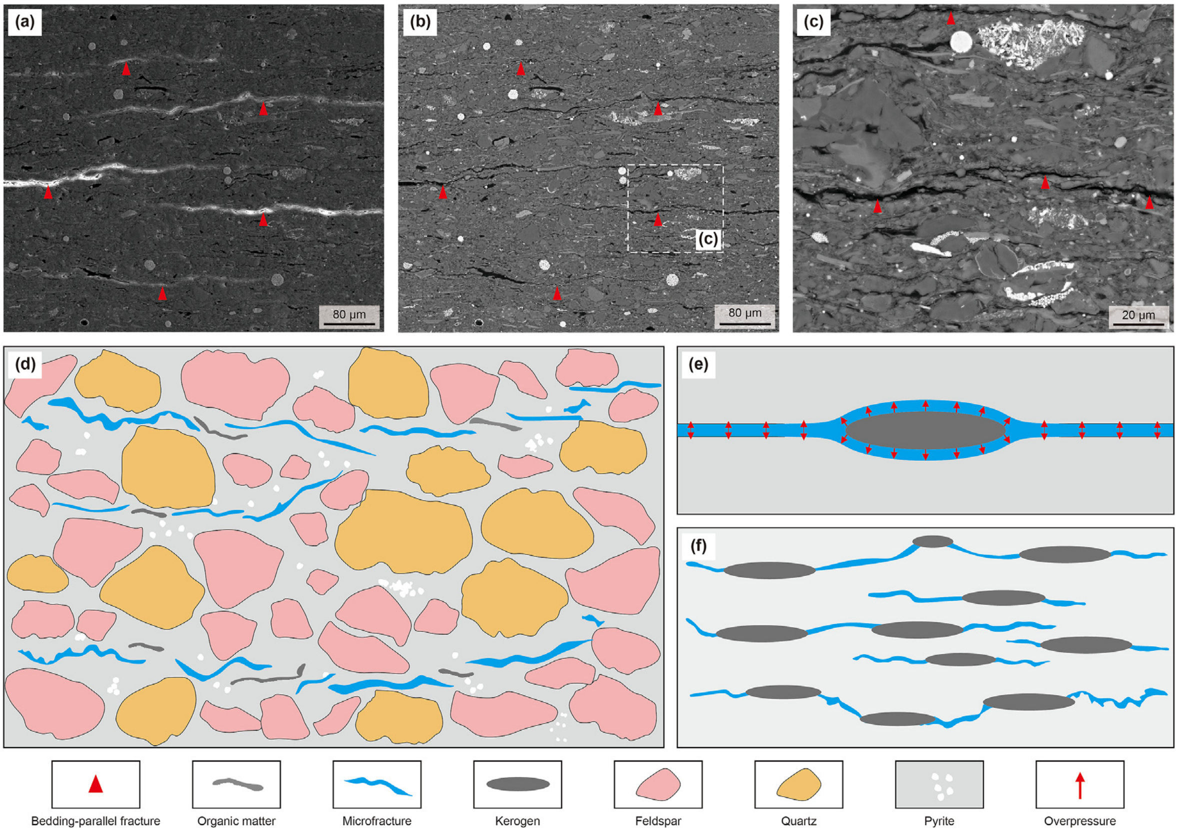

Fig. 14. **(a)** Multiple near-horizontal bedding-parallel fractures, SE image. **(b)** BSE image corresponding to Fig. 14(a). **(c)** Magnified image of Fig. 14(b) showing bedding-parallel fractures distributed near the organic matter. **(d)** Distribution model of bedding-parallel fractures. **(e)** Sketch map of overpressure caused by kerogen maturation. **(f)** Multiple microfractures interconnected to form bedding-parallel fractures.

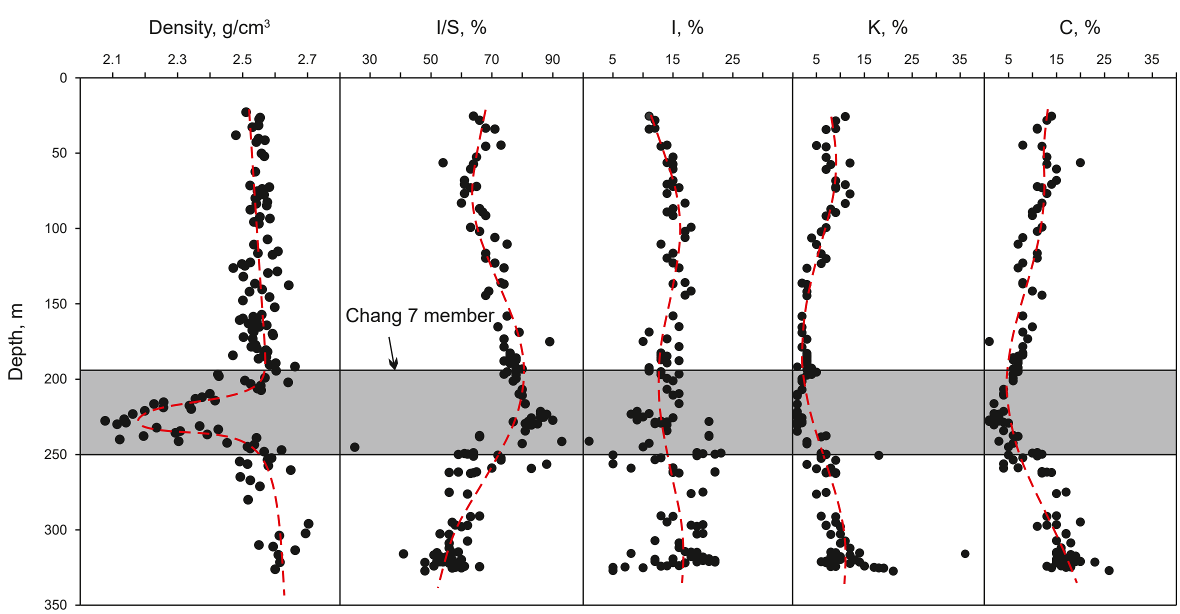

Fig. 15. Vertical distribution of rock density and clay minerals in Well A of the Ordos Basin.

5.3. Effectiveness of natural fractures

Natural fractures under formation conditions must remain open to serve as effective fractures, providing fluid storage space and flow pathways (Gong et al., 2021; Liu et al., 2020a). Previous studies have shown that the present-day tectonic stress field influences the aperture and effectiveness of tectonic fractures, affecting reservoir quality and hydrocarbon production (Du et al., 2023b). The fast shear-wave azimuth in Well B stabilizes at 60°–70°, indicating that the present-day maximum horizontal principal stress (SH_{max}) is

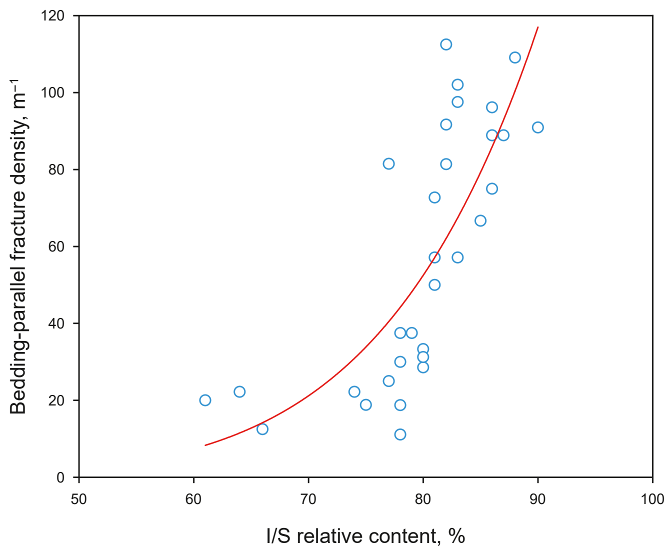

Fig. 16. Relationship between the proportion of mixed-layer illite/smectite and bedding-parallel fracture density.

oriented in the ENE-WSW direction (Fig. 17). The dominant orientation of high-angle tectonic fractures in Well B is NE-SW, intersecting SH_{max} at a small angle (less than 30°), which favors fracture aperture retention. As a result, the tectonic fractures in the study area exhibit good connectivity and permeability.

To assess the contribution of bedding-parallel fractures to the reservoir, we used the test results of organic-rich shale from Well A, as reported by Wang et al. (2023a; their Tables 1 and 3). In these samples, the TOC content exceeded 10 w.t.%. The results show that porosity positively correlates with thermal maturity (R_o), with R_o values ranging from 0.67% to 0.77% and porosity rangig from 0.35% to 3.10% (Fig. 18). When R_o exceeds 0.7%, porosity increases significantly, peaking at 3.10% at the thermal maturity of 0.77%. We attribute this increase in porosity to the maturation of organic matter, which promotes the formation of bedding-parallel fractures. This finding aligns with our earlier discussion that high T_{max} values enhance the development of bedding-parallel fractures. Furthermore, thin section and SEM observations show that the majority of bedding-parallel fractures are unfilled, with apertures ranging from several hundred nanometers to tens of micrometers. Wang et al. (2023a) further demonstrated through gas adsorption and mercury injection experiments that samples with high thermal evolution exhibit larger mesopore and macropore volumes, along with favorable pore-throat configurations (their Fig. 9 and Table 3). Therefore, bedding-parallel fractures can improve pore structure, increase effective porosity, and provide favorable pathways for lateral hydrocarbon migration, thereby enhancing reservoir quality.

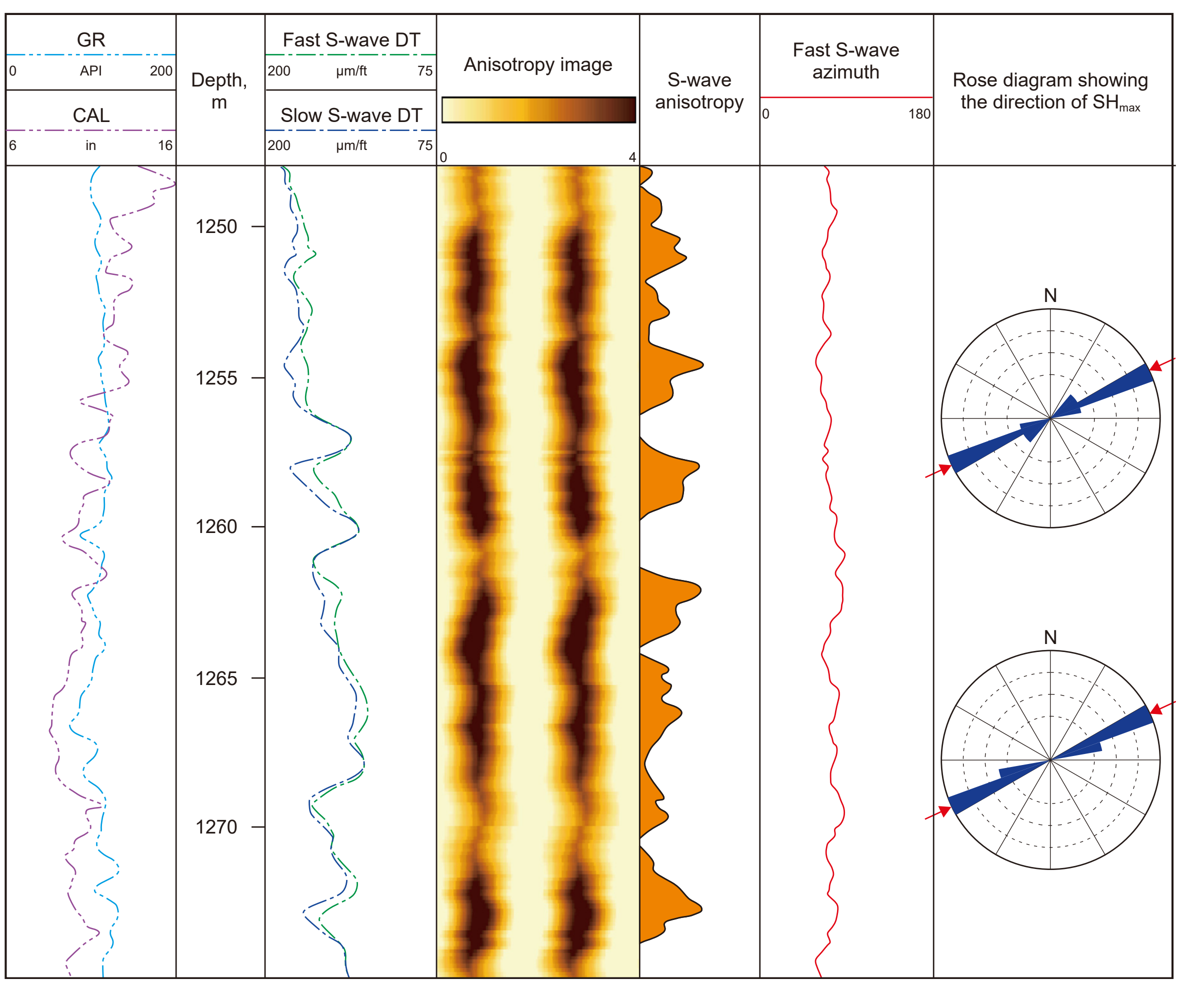

Fig. 17. Anisotropy image of the Chang 7 Member in the Ordos Basin. The fast shear-wave azimuth indicates the direction of the present-day maximum horizontal principal stress (SH_{max}).

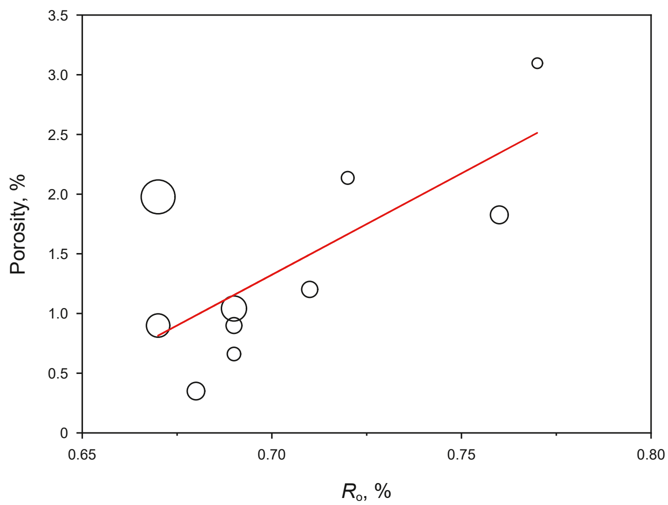

Fig. 18. Relationship between thermal maturity and porosity of the Chang 7 Member, bubble size indicates the TOC content, data from Wang et al. (2023a).

6. Conclusions

Natural fractures in the Chang 7 Member can be categorized into high-angle tectonic fractures and nearly horizontal bedding-parallel fractures. Tectonic fractures typically exhibit high dip angles exceeding 70° and are highly developed, with a single-well fracture density of 2.65 m^{-1}. Bedding-parallel fractures have limited lateral continuity and connectivity, displaying features like branching, bending, or pinching out. Their apertures vary significantly, ranging from hundreds of nanometers to tens of micrometers.

The development of natural fractures is affected by many factors. Siltstone has the highest degree of tectonic fracture development. Which is rich in brittle minerals and strongly cemented by calcite. Tectonic fractures typically occur within the mechanical layers, and their densities are inversely correlated with bed thickness. In contrast, bedding-parallel fractures are primarily found in mudstone. High TOC content and thermal maturity promote the development of bedding-parallel fractures, which are more prevalent in organic-rich and clay lamina. Additionally, the formation of bedding-parallel fractures is attributed to two mechanisms: the conversion of organic matter to hydrocarbons or the transformation of smectite into illite.

Both types of fractures contribute positively to reservoir quality. High-angle tectonic fractures intersect the present-day maximum horizontal principal stress at a small angle, with large apertures and good effectiveness. Bedding-parallel fractures improve pore structure, increase effective porosity, and provide favorable pathways for lateral hydrocarbon migration.

CRediT authorship contribution statement

Xiao-Yu Du: Writing – original draft, Formal analysis, Conceptualization. **Zhi-Jun Jin:** Writing – review & editing, Supervision, Conceptualization. **Lian-Bo Zeng:** Writing – review & editing, Conceptualization. **Guo-Ping Liu:** Visualization, Data curation. **Shi-Xiang Li:** Resources. **Mehdi Ostadhassan:** Writing – review & editing. **Xin-Ping Liang:** Resources, Data curation. **Guan-Ping Wang:** Visualization. **Guo-Qing Lu:** Data curation.

Declaration of competing interest

The authors declare that they have no known competing financial interests or personal relationships that could have appeared to influence the work reported in this paper.

Acknowledgements

This research was supported by the National Natural Science Foundation of China (42090025, 42302148), State Key Laboratory of Shale Oil and Gas Enrichment Mechanisms and Effective Development (33550000-22-ZC0613-0336), and CNPC Innovation Found (2023DQ02-0103). The authors greatly acknowledge the Research Institute of Exploration and Development of PetroChina Changqing Oilfield Company for providing data and other support. We are particularly grateful to the editors and anonymous reviewers for their constructive comments, which contributed significantly to improving this manuscript.

References

Aghli, G., Moussavi-Harami, R., Mohammadian, R., 2019. Reservoir heterogeneity and fracture parameter determination using electrical image logs and petrophysical data (a case study, carbonate Asmari Formation, Zagros Basin, SW Iran). Pet. Sci. 17, 51–69. https://doi.org/10.1007/s12182-019-00413-0.

Al-Ramadan, K., 2013. Illitization of smectite in sandstones: the permian unayzah reservoir, Saudi arabia. Arabian J. Sci. Eng. 39, 407–412. https://doi.org/10.1007/s13369-013-0913-6.

Altindag, R., 2010. Reply to the discussion by yagiz on “assessment of some brittleness indexes in rock-drilling efficiency” by altindag. Rock Mech. Rock Eng. 43, 375–376. https://doi.org/10.1007/s00603-009-0079-4.

Anders, M.H., Laubach, S.E., Scholz, C.H., 2014. Microfractures: a review. J. Struct. Geol. 69, 377–394. https://doi.org/10.1016/j.jsg.2014.05.011.

Bowker, K.A., 2007. Barnett shale gas production, fort worth basin: issues and discussion. AAPG Bull. 91, 523–533. https://doi.org/10.1306/06190606018.

Bruce, C.H., 1984. Smectite dehydration—its relation to structural development and hydrocarbon accumulation in northern Gulf of Mexico Basin1. AAPG Bull. 68, 673–683. https://doi.org/10.1306/AD461363-16F7-11D7-8645000102C1865D.

Cao, Y., Jin, Z.J., Zhu, R.K., Liu, K.Q., 2023. Microstructures of continental organic-rich shale and its adjacent siltstone and carbonate rocks—an example from the Lucaogou Formation, Jimusar Sag, Junggar Basin, NW China. Geoenergy Sci. Eng. 225, 211705. https://doi.org/10.1016/j.geoen.2023.211705.

Cao, Y., Jin, Z.J., Zhu, R.K., Liu, K.Q., Bai, J.N., 2024. Comprehensive evaluation of the organic-rich saline lacustrine shale in the Lucaogou Formation, Jimusar sag, Junggar Basin, NW China. Energy 294, 130786. https://doi.org/10.1016/j.energy.2024.130786.

Capuano, R.M., 1993. Evidence of fluid flow in microfractures in geopressured shales. AAPG Bull. 77, 1303–1314. https://doi.org/10.1306/BDFF8E70-1718-11D7-8645000102C1865D.

Chalmers, G.R., Bustin, R.M., Power, I.M., 2012. Characterization of gas shale pore systems by porosimetry, pycnometry, surface area, and field emission scanning electron microscopy/transmission electron microscopy image analyses: examples from the Barnett, Woodford, Haynesville, Marcellus, and Doig units. AAPG Bull. 96, 1099–1119. https://doi.org/10.1306/10171111052.

Chen, G., Chang, X.C., Gang, W.Z., Wang, N., Zhang, P.F., Cao, Q.Y., Xu, J.B., 2020. Anomalous positive pyrite sulfur isotope in lacustrine black shale of the Yanchang Formation, Ordos Basin: triggered by paleoredox chemistry changes. Mar. Petrol. Geol. 121, 104587. https://doi.org/10.1016/j.marpetgeo.2020.104587.

Cobbold, P.R., Zanella, A., Rodrigues, N., Løseth, H., 2013. Bedding-parallel fibrous veins (beef and cone-in-cone): worldwide occurrence and possible significance in terms of fluid overpressure, hydrocarbon generation and mineralization. Mar. Petrol. Geol. 43, 1–20. https://doi.org/10.1016/j.marpetgeo.2013.01.010.

Cooke, M.L., Simo, J.A., Underwood, C.A., Rijken, P., 2006. Mechanical stratigraphic controls on fracture patterns within carbonates and implications for groundwater flow. Sediment. Geol. 184, 225–239. https://doi.org/10.1016/j.sedgeo.2005.11.004.

Cui, J.W., Zhu, R.K., Luo, Z., Li, S., 2019. Sedimentary and geochemical characteristics of the triassic Chang 7 member shale in the Southeastern Ordos Basin, Central China. Pet. Sci. 16, 285–297. https://doi.org/10.1007/s12182-019-0307-9.

Curtis, J.B., 2002. Fractured shale-gas systems. AAPG Bull. 86, 1921–1938. https://doi.org/10.1306/61eeddbe-173e-11d7-8645000102c1865d.

Day-Stirrat, R.J., Aplin, A.C., Środoń, J., van der Pluijm, B.A., 2008. Diagenetic reorientation of phyllosilicate minerals in Paleogene mudstones of the podhale basin, southern Poland. Clays Clay Miner. 56, 100–111. https://doi.org/10.1346/ccmn.2008.0560109.

Ding, W.L., Li, C., Li, C.Y., Xu, C.C., Jiu, K., Zeng, W.T., Wu, L.M., 2012. Fracture

development in shale and its relationship to gas accumulation. Geosci. Front. 3, 97–105. https://doi.org/10.1016/j.gsf.2011.10.001.
Du, X.Y., Jin, Z.J., Zeng, L.B., Liu, G.P., He, W.J., Ostadhassan, M., Liang, X.P., Yang, S., Lu, G.Q., 2023a. Characteristics and controlling factors of natural fractures in deep lacustrine shale oil reservoirs of the Permian Fengcheng Formation in the Mahu Sag, Junggar Basin, China. J. Struct. Geol. 175, 104923. https://doi.org/10.1016/j.jsg.2023.104923.
Du, X.Y., Jin, Z.J., Zeng, L.B., Liu, G.P., He, W.J., Ostadhassan, M., Song, Y., Liang, X.P., Yang, S., Lu, G.Q., 2023b. Formation of natural fractures and their impact on shale oil accumulation in the Mahu Sag, Junggar Basin, NW China. Int. J. Coal Geol. 279, 104385. https://doi.org/10.1016/j.coal.2023.104385.
English, J.M., 2012. Thermomechanical origin of regional fracture systems. AAPG Bull. 96, 1597–1625. https://doi.org/10.1306/01021211018.
Fan, Z.Q., Jin, Z.H., Johnson, S.E., 2010. Subcritical propagation of an oil-filled penny-shaped crack during kerogen-oil conversion. Geophys. J. Int. 182, 1141–1147. https://doi.org/10.1111/j.1365-246X.2010.04689.x.
Fu, S.T., Jin, Z.J., Fu, J.H., Li, S.X., Yang, W.W., 2021. Transformation of understanding from tight oil to shale oil in the Member 7 of Yanchang Formation in Ordos Basin and its significance of exploration and development. Acta Petrolei Sinica 42, 561–569. https://doi.org/10.7623/syxb202105001 (in Chinese).
Fu, J.H., Li, S.X., Niu, X.B., Deng, X.Q., Zhou, X.P., 2020. Geological characteristics and exploration of shale oil in Chang 7 member of triassic Yanchang Formation, Ordos Basin, NW China. Petrol. Explor. Dev. 47, 931–945. https://doi.org/10.1016/s1876-3804(20)60107-0.
Gale, J.F.W., Laubach, S.E., Olson, J.E., Eichhubl, P., Fall, A., 2014. Natural Fractures in shale: a review and new observations. AAPG Bull. 98, 2165–2216. https://doi.org/10.1306/08121413151.
Gale, J.F.W., Reed, R.M., Holder, J., 2007. Natural fractures in the Barnett Shale and their importance for hydraulic fracture treatments. AAPG Bull. 91, 603–622. https://doi.org/10.1306/11010606061.
Ghosh, S., Galvis-Portilla, H.A., Klockow, C.M., Slatt, R.M., 2018. An application of outcrop analogues to understanding the origin and abundance of natural fractures in the Woodford Shale. J. Pet. Sci. Eng. 164, 623–639. https://doi.org/10.1016/j.petrol.2017.11.073.
Ghosh, K., Mitra, S., 2009. Two-dimensional simulation of controls of fracture parameters on fracture connectivity. AAPG Bull 93, 1517–1533. https://doi.org/10.1306/07270909041.
Gong, L., Fu, X.F., Wang, Z.S., Gao, S., Jabbari, H., Yue, W.T., Liu, B., 2019. A new approach for characterization and prediction of natural fracture occurrence in tight oil sandstones with intense anisotropy. AAPG Bull. 103, 1383–1400. https://doi.org/10.1306/12131818054.
Gong, L., Wang, J., Gao, S., Fu, X.F., Liu, B., Miao, F.B., Zhou, X.P., Meng, Q.K., 2021. Characterization, controlling factors and evolution of fracture effectiveness in shale oil reservoirs. J. Pet. Sci. Eng. 203, 108655. https://doi.org/10.1016/j.petrol.2021.108655.
Gottardi, R., Mason, S.L., 2018. Characterization of the natural fracture system of the eagle ford formation (val verde county, Texas). AAPG Bull. 102, 1963–1984. https://doi.org/10.1306/03151817323.
Heidari, M., Khanlari, G.R., Torabi-Kaveh, M., Kargarian, S., Saneie, S., 2013. Effect of porosity on rock brittleness. Rock Mech. Rock Eng. 47, 785–790. https://doi.org/10.1007/s00603-013-0400-0.
Hooker, J.N., Laubach, S.E., Marrett, R., 2013. Fracture-aperture size—frequency, spatial distribution, and growth processes in strata-bounded and non-strata-bounded fractures, Cambrian Mesón Group, NW Argentina. J. Struct. Geol. 54, 54–71. https://doi.org/10.1016/j.jsg.2013.06.011.
Hou, L.H., Wu, S.T., Jing, Z.H., Jiang, X.H., Yu, Z.C., Hua, G.L., Su, L., Yu, C., Liao, F.R., Tian, H., 2022. Effects of types and content of clay minerals on reservoir effectiveness for lacustrine organic matter rich shale. Fuel 327, 125043. https://doi.org/10.1016/j.fuel.2022.125043.
Jarvie, D.M., 2012. Shale resource systems for oil and gas: Part 2—shale-oil resource systems. In: Breyer, J.A. (Ed.), Shale Reservoirs—Giant Resources for the 21st Century, vol. 97. AAPG Memoir, pp. 89–119. https://doi.org/10.1306/13321447M973489.
Jiang, M.M., Fu, X.F., Wang, Z.C., 2023. An experimental investigation of the characteristics of cataclastic bands in high-porosity sandstones. Geol. Soc. Am. Bull. 136, 3069–3084. https://doi.org/10.1130/b36801.1.
Jin, Z.J., Zhu, R.K., Liang, X.P., Shen, Y.Q., 2021. Several issues worthy of attention in current lacustrine shale oil exploration and development. Petrol. Explor. Dev. 48, 1471–1484. https://doi.org/10.1016/s1876-3804(21)60303-8.
Jiu, B., Huang, W.H., Mu, N.N., 2022. Mineralogy and elemental geochemistry of Permo-Carboniferous Li-enriched coal in the southern Ordos Basin, China: implications for modes of occurrence, controlling factors and sources of Li in coal. Ore Geol. Rev. 141, 104686. https://doi.org/10.1016/j.oregeorev.2021.104686.
Ju, W., Niu, X.B., Feng, S.B., You, Y., Xu, K., Wang, G., Xu, H.R., 2020. Predicting the present-day in situ stress distribution within the Yanchang Formation Chang 7 shale oil reservoir of Ordos Basin, central China. Pet. Sci. 17, 912–924. https://doi.org/10.1007/s12182-020-00448-8.
Lai, J., Liu, B.C., Li, H.B., Pang, X.J., Liu, S.C., Bao, M., Wang, G.W., 2022. Bedding parallel fractures in fine-grained sedimentary rocks: recognition, formation mechanisms, and prediction using well log. Pet. Sci. 19, 554–569. https://doi.org/10.1016/j.petsci.2021.10.017.
Lash, G.G., Engelder, T., 2005. An analysis of horizontal microcracking during catagenesis: example from the Catskill delta complex. AAPG Bull. 89, 1433–1449. https://doi.org/10.1306/05250504141.
Laubach, S.E., Olson, J.E., Gross, M.R., 2009. Mechanical and fracture stratigraphy. AAPG Bull. 93, 1413–1426. https://doi.org/10.1306/07270909094.
Li, S., Zhu, R.K., Cui, J.W., Luo, Z., Cui, J.G., Liu, H., Li, W.Q., 2019. The petrological characteristics and significance of organic-rich shale in the Chang 7 member of the Yanchang Formation, south margin of the Ordos basin, central China. Pet. Sci. 16, 1255–1269. https://doi.org/10.1007/s12182-019-00386-0.
Liu, G.P., Zeng, L.B., Li, H.N., Ostadhassan, M., Rabiei, M., 2020a. Natural fractures in metamorphic basement reservoirs in the Liaohe Basin, China. Mar. Petrol. Geol. 119, 104479. https://doi.org/10.1016/j.marpetgeo.2020.104479.
Liu, G.P., Zeng, L.B., Sun, G.Q., Zu, K.W., Qin, L.B., Mao, Z., Ostadhassan, M., 2020b. Natural fractures in tight gas volcanic reservoirs and their influences on production in the Xujiaweizi depression, Songliao Basin, China. AAPG Bull. 104, 2099–2123. https://doi.org/10.1306/05122017169.
Liu, H.L., Qiu, Z., Zou, C.N., Fu, J.H., Zhang, W.Z., Tao, H.F., Li, S.X., Zhou, S.W., Wang, L., Chen, Z.Q., 2021a. Environmental changes in the Middle Triassic lacustrine basin (Ordos, North China): implication for biotic recovery of freshwater ecosystem following the Permian-Triassic mass extinction. Global Planet. Change 204, 103559. https://doi.org/10.1016/j.gloplacha.2021.103559.
Liu, J.S., Ding, W.L., Yang, H.M., Liu, Y., 2021b. Quantitative multiparameter prediction of fractured tight sandstone reservoirs: a case study of the Yanchang Formation of the Ordos Basin, Central China. SPE J. 26, 3342–3373. https://doi.org/10.2118/205495-pa.
Liu, J.D., Liu, T., Liu, H., He, L., Zheng, L.J., 2021c. Overpressure caused by hydrocarbon generation in the organic-rich shales of the Ordos Basin. Mar. Petrol. Geol. 134, 105349. https://doi.org/10.1016/j.marpetgeo.2021.105349.
Liu, Q.Y., Li, P., Jin, Z.J., Sun, Y.W., Hu, G., Zhu, D.Y., Huang, Z.K., Liang, X.P., Zhang, R., Liu, J.Y., 2021d. Organic-rich formation and hydrocarbon enrichment of lacustrine shale strata: a case study of Chang 7 Member. Sci. China Ear. Sci. 65, 118–138. https://doi.org/10.1007/s11430-021-9819-y.
Lyu, W.Y., Zeng, L.B., Zhou, S.B., Du, X.S., Xia, D.L., Liu, G.P., Li, J., Weng, J.Q., 2019. Natural fractures in tight-oil sandstones: a case study of the upper Triassic Yanchang Formation in the southwestern Ordos Basin, China. AAPG Bull. 103, 2343–2367. https://doi.org/10.1306/0130191608617115.
McGinnis, R.N., Ferrill, D.A., Morris, A.P., Smart, K.J., Lehrmann, D., 2017. Mechanical stratigraphic controls on natural fracture spacing and penetration. J. Struct. Geol. 95, 160–170. https://doi.org/10.1016/j.jsg.2017.01.001.
Meng, Q.F., Hao, F., Tian, J.Q., 2021. Origins of non-tectonic fractures in shale. Earth Sci. Rev. 222, 103825. https://doi.org/10.1016/j.earscirev.2021.103825.
Momper, J.A., 1979. Generation of abnormal pressures through organic matter transformations. AAPG Bull. 63, 1424. https://doi.org/10.1306/2F918568-16CE-11D7-8645000102C1865D.
Ortega, O.J., Marrett, R.A., Laubach, S.E., 2006. A scale-independent approach to fracture intensity and average spacing measurement. AAPG Bull. 90, 193–208. https://doi.org/10.1306/08250505059.
Ougier-Simonin, A., Renard, F., Boehm, C., Vidal-Gilbert, S., 2016. Microfracturing and microporosity in shales. Earth Sci. Rev. 162, 198–226. https://doi.org/10.1016/j.earscirev.2016.09.006.
Pang, X.J., Wang, G.W., Kuang, L.C., Zhao, F., Li, C.L., Wang, C.Y., Zhang, M., Lai, J., 2023. Lamellation fractures in shale oil reservoirs: recognition, prediction and their influence on oil enrichment. Mar. Petrol. Geol. 148, 106032. https://doi.org/10.1016/j.marpetgeo.2022.106032.
Powers, M.C., 1967. Fluid-release mechanisms in compacting marine mudrocks and their importance in oil Exploration1. AAPG Bull. 51, 1240–1254. https://doi.org/10.1306/5D25C137-16C1-11D7-8645000102C1865D.
Qin, X., Han, D.H., Zhao, L.X., 2019. Elastic characteristics of overpressure due to smectite-to-illite transition based on micromechanism analysis. Geophysics 84, WA23–WA42. https://doi.org/10.1190/geo2018-0338.1.
Shi, J.X., Zeng, L.B., Zhao, X.Y., Zhang, Y.Z., Wang, J.P., 2020. Characteristics of natural fractures in the upper Paleozoic coal bearing strata in the southern Qinshui Basin, China: implications for coalbed methane (CBM) development. Mar. Petrol. Geol. 113, 104152. https://doi.org/10.1016/j.marpetgeo.2019.104152.
Shi, J.X., Zhao, X.Y., Zeng, L.B., Zhang, Y.Z., Zhu, Z.P., Dong, S.Q., 2023. Identification of reservoir types in deep carbonates based on mixed-kernel machine learning using geophysical logging data. Pet. Sci. 21, 1632–1648. https://doi.org/10.1016/j.petsci.2023.12.016.
Sun, L.D., Liu, H., He, W.Y., Li, G.X., Zhang, S.C., Zhu, R.K., Jin, X., Meng, S.W., Jiang, H., 2021. An analysis of major scientific problems and research paths of Gulong shale oil in Daqing Oilfield, NE China. Petrol. Explor. Dev. 48, 527–540. https://doi.org/10.1016/s1876-3804(21)60043-5.
Vernik, L., 1994. Hydrocarbon-generation-induced microcracking of source rocks. Geophysics 59, 555–563. https://doi.org/10.1190/1.1443616.
Wang, G.P., Jin, Z.J., Zhang, Q., Zhu, R.K., Tang, X., Liu, K.Q., Dong, L., 2023a. Effects of clay minerals and organic matter on pore evolution of the early mature lacustrine shale in the Ordos Basin, China. J. Asian Earth Sci. 246, 105516. https://doi.org/10.1016/j.jseaes.2022.105516.
Wang, G.P., Zhang, Q., Zhu, R.K., Tang, X., Liu, K.Q., Jin, Z.J., 2023b. Geological controls on the pore system of lacustrine unconventional shale reservoirs: the Triassic Chang 7 member in the Ordos Basin, China. Geoenergy Sc. Eng. 221, 111139. https://doi.org/10.1016/j.petrol.2022.111139.
Wang, R.Y., Ding, W.L., Zhang, Y.Q., Wang, Z., Wang, X.H., He, J.H., Zeng, W.T., Dai, P., 2016. Analysis of developmental characteristics and dominant factors of fractures in Lower Cambrian marine shale reservoirs: a case study of Niutitang formation in Cen'gong block, southern China. J. Pet. Sci. Eng. 138, 31–49. https://doi.org/10.1016/j.petrol.2015.12.004.
Xi, K.L., Li, K., Cao, Y.C., Lin, M.R., Niu, X.B., Zhu, R.K., Wei, X.Z., You, Y., Liang, X.W.,

Feng, S.B., 2020. Laminae combination and shale oil enrichment patterns of Chang 73 sub-member organic-rich shales in the Triassic Yanchang Formation, Ordos Basin, NW China. Petrol. Explor. Dev. 47, 1342–1353. https://doi.org/10.1016/s1876-3804(20)60142-8.

Yang, Y.F., Mavko, G., 2018. Mathematical modeling of microcrack growth in source rock during kerogen thermal maturation. AAPG Bull. 102, 2519–2535. https://doi.org/10.1306/05111817062.

Yang, Z., Hou, L.H., Tao, S.Z., Cui, J.W., Wu, S.T., Lin, S.H., Pan, S.Q., 2015. Formation and "sweet area" evaluation of liquid-rich hydrocarbons in shale strata. Petrol. Explor. Dev. 42, 609–620. https://doi.org/10.1016/s1876-3804(15)30056-2.

Yang, Z., Zou, C.N., Hou, L.H., Wu, S.T., Lin, S.H., Luo, X., Zhang, L.J., Zhao, Z.Y., Cui, J.W., Pan, S.Q., 2019. Division of fine-grained rocks and selection of "sweet sections" in the oldest continental shale in China: taking the coexisting combination of tight and shale oil in the Permian Junggar Basin. Mar. Petrol. Geol. 109, 339–348. https://doi.org/10.1016/j.marpetgeo.2019.06.010.

Yao, J.L., Zhao, Y.D., Liu, G.L., Qi, Y.L., Li, Y.H., Luo, A.X., Zhang, X.L., 2018. Formation patterns of Chang 9 oil reservoir in triassic Yanchang Formation, Ordos Basin, NW China. Petrol. Explor. Dev. 45, 389–401. https://doi.org/10.1016/s1876-3804(18)30044-2.

Zeng, L.B., He, Y.H., Xiong, W.L., 2010. Origin and geological significance of the cross fractures in the upper triassic Yanchang Formation, Ordos Basin, China. Energy Explor. Exploit. 28, 59–70. https://doi.org/10.1260/0144-5987.28.2.59.

Zeng, L.B., Lyu, W.Y., Li, J., Zhu, L.F., Weng, J.Q., Yue, F., Zu, K., 2016. Natural fractures and their influence on shale gas enrichment in Sichuan Basin, China. J. Nat. Gas Sci. Eng. 30, 1–9. https://doi.org/10.1016/j.jngse.2015.11.048.

Zeng, L.B., Xu, X., Ma, S.J., Bao, H.Y., Tian, H., Mao, Z., Ostadhassan, M., Dong, S.Q., Lyu, W.Y., 2023a. Contribution of lamellation fractures to porosity and permeability of shales: a case study of the Jiaoshiba area in the Sichuan Basin, China. Geoenergy Sci. Eng. 232, 212439. https://doi.org/10.1016/j.geoen.2023.212439.

Zeng, X., Yang, T., Feng, J.W., Bian, C.S., Guan, M., Liu, W., Guo, B.C., Dong, J., 2023b. Development characteristics and controlling factors of fractures in lacustrine shale and their geological significance for evaluating shale oil sweet spots in the third member of the Shahejie Formation in the Qikou Sag, Bohai Bay basin. Pet. Sci. 21, 791–805. https://doi.org/10.1016/j.petsci.2023.10.029.

Zhang, W.Z., Xie, L.Q., Yang, W.W., Qin, Y., Peng, P.A., 2017. Micro fractures and pores in lacustrine shales of the upper triassic Yanchang Chang7 member, Ordos Basin, China. J. Pet. Sci. Eng. 156, 194–201. https://doi.org/10.1016/j.petrol.2017.03.044.

Zhang, X.M., Shi, W.Z., Hu, Q.H., Zhai, G.Y., Wang, R., Xu, X.F., Meng, F.L., Liu, Y.Z., Bai, L.H., 2020. Developmental characteristics and controlling factors of natural fractures in the lower paleozoic marine shales of the upper Yangtze Platform, southern China. J. Nat. Gas Sci. Eng. 76. https://doi.org/10.1016/j.jngse.2020.103191.

Zhao, W.T., Hou, G.T., 2017. Fracture prediction in the tight-oil reservoirs of the Triassic Yanchang Formation in the Ordos Basin, northern China. Petr. Sci. 14, 1–23. https://doi.org/10.1007/s12182-016-0141-2.

Zhao, W.T., Hou, G.T., Hari, K.R., 2016. Two episodes of structural fractures and their stress field modeling in the Ordos Block, northern China. J. Geodyn. 97, 7–21. https://doi.org/10.1016/j.jog.2016.02.005.

Zhao, X.Y., He, D.B., 2012. Clay minerals and shale gas. Xinjiang Pet. Geol. 33, 643–647 (in Chinese).

Zou, C.N., Yang, Z., Cui, J.W., Zhu, R.K., Hou, L.G., Tao, S.Z., Yuan, X.H., Wu, S.T., Lin, S.H., Wang, L., Bai, B., Yao, J.L., 2013. Formation mechanism, geological characteristics and development strategy of nonmarine shale oil in China. Petrol. Explor. Dev. 40, 15–27. https://doi.org/10.1016/s1876-3804(13)60002-6.